The reduction of operational amplifier electrical outputs to improve piezoelectric shunts with negative capacitance

M. Berardengo[1], S. Manzoni[2], O. Thomas[3], C. Giraud-Audine[4], L. Drago[2], S. Marelli[2], M. Vanali[5]

1. Università degli Studi di Genova - Department of Mechanical, Energy, Management and Transportation Engineering, Via Opera Pia, 15A - 16145 Genoa (Italy)
2. Politecnico di Milano – Department of Mechanical Engineering Via La Masa, 34 – 20156 Milan (Italy)
3. Arts et Métiers Institute of Technology, LISPEN, HESAM Université, F-59000 Lille, France
4. Arts et Métiers Institute of Technology, Univ. Lille, Centrale Lille, HEI, HESAM Université, EA 2697 - L2EP, F-59000 Lille, France
5. Università degli Studi di Parma - Department of Engineering and Architecture Parco Area delle Scienze, 181/A – 43124 Parma (Italy)

Corresponding author: Stefano Manzoni

Phone: +390223998589

e-mail: stefano.manzoni@polimi.it

ABSTRACT

One way to enhance the performance of vibration control with piezoelectric shunt is to use a negative capacitance in the shunt circuit. This component is very effective and provides good results in terms of attenuation improvement without significantly increasing the complexity of the shunt network. However, negative capacitances are built using operational amplifiers and, in some applications, the risk of saturation of the outputs of the operational amplifier exists. This constitutes a non-negligible aspect since it leads to a non-proper functioning of the control system which significantly deteriorates the control performance or even triggers instability phenomena. In light of this limitation, this paper proposes strategies to decrease the outputs of the operational amplifier in order to reduce the risk of saturation acting just on the values of the circuit components, without worsening the attenuation performance. However, when the achievable reduction is not sufficient, it is also possible to act on other components accepting a deterioration of the attenuation performance. Guidelines are provided for properly choosing the best shunt circuit configuration accounting for both the extent of the operational amplifier outputs and the control performance. The paper also evidences that the mechanical part of the system cannot be neglected in the analysis when assessing the operational amplifier outputs. Furthermore, two different circuit types used to build the negative capacitance are compared in terms of output requirements. This analysis shows that there is no circuit always less demanding than the other and that the choice of the circuit is not always straightforward. Therefore, a multi-degree of freedom model is presented, which is essential to understand

which configuration of the negative capacitance has to be used in a given engineering application. All the presented outcomes are validated through an experimental campaign.

KEYWORDS: Piezoelectric shunt, resistive shunt, negative capacitance, saturation, damping, operational amplifier, vibration attenuation

1. Introduction

The use of piezoelectric shunt for attenuating vibrations in light structures is a well-known technique where piezoelectric transducers act at the same time as both sensors and actuators, and which has been extensively studied and employed in engineering applications (e.g. hard-disk vibrations [1], vibrations of turbine blades [2,3]). Piezoelectric shunt usually consists in the electrical connection between a piezoelectric transducer bonded to the vibrating structure and a properly designed passive electrical network [4–8]. According to the layout of the electrical network, it is possible to perform mono-modal control (e.g. [9–14]) or multi-mode control with either single (e.g. [15–19]) or multiple piezoelectric transducers (e.g. [20,21]). Hence, in the classical approach, the piezoelectric shunt damping is a passive technique and does not imply the use of either expensive electronic devices or real-time controllers. On the one hand, this represents an advantage making the control system inexpensive, stable and easy to be implemented. On the other hand, the power involved is limited and the control performances are lower if compared to the traditional active control strategies [22].

An effective approach for improving the control performance of the piezoelectric shunt is the addition of synthetic circuits in the shunt impedance (e.g. [23–29]), even in a context of periodic structures (e.g. [30,31]). This is a technique often employed also in other smart control approaches like, as an example, electro-magnetic shunt (e.g. [32–34]). In all these cases, the use of synthetic circuits showed to provide significant improvement in terms of vibration attenuation performance (e.g. [35]). However, in these cases, due to the presence in the circuit of components which have to be supplied, the approach becomes semi-active.

Among the approaches which rely on additional synthetic circuits in piezoelectric shunt, the use of negative capacitances (NC) has been shown to be reliable and effective. The addition of NCs proved to be able to artificially increase the modal electro-mechanical coupling factor for all the modes of a system. This coupling factor is one of the main parameters affecting the control performance since it is representative of the efficiency of the conversion between mechanical and electrical energy (i.e. the increase of the absolute value of the modal electro-mechanical coupling factor related to the i^{th} mode, k_i, increases the achievable attenuation level on the corresponding mode) [6,36]. For this reason, NCs can be successfully applied to improve the effectiveness of any type of passive shunt circuit. In this scenario, their use becomes attractive especially when they are coupled to simple shunt impedances, allowing for both good attenuation levels and easy-to-implement systems at the same time. Even if the NCs can be coupled to any passive shunt impedance, many works in the literature have focused on the coupling of NCs to resistive (e.g. [22,37–41]) and resonant shunt impedances (e.g. [22,42–44]). A resistive impedance is made from a single resistance, while a resonant impedance is made from either the parallel or the series of an inductance and a resistance. When no NCs are used, the tuned resonant shunt offers attenuation levels much higher than the resistive shunt, but, when NCs are added in the shunt circuit, the attenuation provided by the resistive shunt becomes closer and closer to that of the resonant shunt [45]. Former studies already proved that resonant shunt shows low robustness to system changes and uncertainties (e.g. [12,46–48]). Conversely, the resistive shunt coupled to NCs shows to be highly robust [45] and able to damp more than one mode at the same time [38,45,49].

Considering the aforementioned reasons, the piezoelectric shunt based on resistive impedances coupled to NCs is a very effective, reliable, inexpensive and easy-to-implement approach to damp vibrations. The main issue of this approach is related to possible dynamic instabilities of the electro-mechanical system (composed by the vibrating structure, the piezoelectric actuator and the shunt impedance) due to the active nature of the NCs. Indeed, since NCs do not exist in nature, they are implemented by using operational amplifiers (OP-AMP) [50] and this makes the control approach semi-active, as mentioned. This problem has been widely studied in the literature and different works provide the limits on the NC value to avoid instability (e.g. [22,42,49]). Nevertheless, there is also another important problem: the OP-AMPs can undergo to saturation of their outputs, thus leading to a non-proper functioning of the control system, and sometimes triggering instability phenomena [49,51]. This problem is not deepened in the literature but it is very important because it limits the applicability and the reliability of the piezoelectric shunt based on NCs.

The most intuitive approach to overcome the aforementioned problem is to use high power amplifiers, but this increases significantly the cost of the control system and, in case of an increase of the disturbance forces acting on the mechanical system, saturation can still occur. Another possibility is to use more complex circuits simulating NCs (e.g. [26]); even if the approach is effective, the complexity of the shunt circuit increases significantly. Therefore, different researchers have studied whether it is possible to decrease the output of the OP-AMP without changing the traditional layout of the NC circuit. Beck et al. [51] described how the different electric elements (i.e. resistances and capacitances) present in the NC circuit are able to change (i.e. increase/decrease) the OP-AMP voltage and power output as a function of the frequency in the case of an NC connected in series to the shunt resistance and the piezoelectric actuator. Qureshi et al. [52] proposed a similar study, but considering a resonant shunt coupled to an NC. Other related works are those of Václavíc et al., who studied the energy flow in applications related to vibration isolation using NCs connected in series to the shunt resistance and the piezoelectric actuator [53] and proposed the use of switching amplifers to decrease the electric power consumption of the shunt control [54]. Even if the referenced works provided a significant insight of the problem, there are still open points to be addressed.

Under a general point of view, the main target of most of the referenced works is to study the dependence of the OP-AMP outputs on the values of the components of the NC circuit (i.e. resistances and capacitances) and the shunt impedance. On the one hand, this approach shows whether it is possible to act on the circuit parameters to reduce the OP-AMP outputs but, on the other hand, it loses sight of the main target of the piezoelectric shunt damping, that is the vibration attenuation. These studies, indeed, do not evidence either how a reduction of the OP-AMP output, achieved by changing the values of the circuit parameters, affects the control effectiveness or whether it is possible to achieve the reduction of the OP-AMP output mantaining a given control performance. Furthermore, the main focus of the analyses in the literature is on the effect of the electrical part of the electro-mechanical system on the OP-AMP outputs, while the effect of the dynamics of the mechanical system is not deepened.

In this scenario, this paper aims to fill some of these gaps in order to provide a more general overview of the problem. Particularly: (i) the electro-mechanical system will be considered not just under the electrical point of view but also the mechanical part will be taken into account in the analysis, showing how the dynamics of a multi-degree-of-freedom (MDOF) mechanical system is able to influence the OP-AMP output; (ii) an analysis aiming at investigating whether and how it is possible to decrease the demand on the OP-AMP outputs given a certain level of vibration reduction will be presented. It will be shown that some electric parameters can be tuned in order to decrease the OP-AMP outputs without changing the attenuation performance provided by the shunt. Furthermore, this analysis will be shown to be general and not dependent on the type of passive shunt impedance coupled to the NC. This analysis will also evidence that it is possible to act separately on the voltage and current outputs of the OP-AMP, with the consequent possibility to lower the power consumption of the NC circuit; (iii) without the constraint of maintaining

constant the level of vibration attenuation, a further analysis will be performed to evidence the effect of the circuit parameters on both the OP-AMP outputs and the attenuation performance; (iv) it is well-known that there are different ways to connect the piezoelectric actuator to the NC and the resistance (the classical series and parallel connections will be taken into account here) and there are also different circuits to build NCs. The paper will analyse all these different cases, providing a detailed description of the OP-AMP outputs in the different configurations. This will allow for direct comparisons among the different solutions and will provide useful information about which configuration must be preferred in given practical cases; (v) based on the above points, the paper provides general guidelines on how to build an NC according to given targets in terms of both OP-AMP outputs and attenuation performance.

The paper is structured as follows: Section 2 will present the model of the electro-mechanical system used in this paper and the circuits adopted for building the NCs. Section 3 will explain how the OP-AMP outputs can be changed without changing the attenuation performance, and will discuss the different possible layouts of the shunt impedance. Section 4 will show how the mechanical behaviour of the electro-mechanical system influences the OP-AMP outputs. The results of this section will also allow to show the effects of the parameters able to change at the same time the OP-AMP outputs and the attenuation performance. Section 5 proposes an MDOF model of the electro-mechanical system, that is needed for assessing which NC layout should be preferred in a given specific engineering application. Section 6 provides guidelines on how to build the shunt impedance according to given targets in terms of both OP-AMP outputs and attenuation performance. Finally, Section 7 will present the experiments carried out to validate the previous theoretical results.

2. The model of the electro-mechanical system and the implementation of the NC

2.1 The model of the electro-mechanical system

The model used in this paper was originally developed by Thomas et al. [6,55] and Ducarne et al. [56], and then refined by Berardengo et al. [49]. Here, the model is briefly recalled for the sake of clarity in order to provide the basics needed for the comprehension of this work. The interested reader can find more details in the referenced articles.

A generic structure is excited by an external forcing F and a piezoelectric actuator, bonded to the structure, is shunted with an electric impedance Z_{sh} (see Figure 1). Q is the charge in one electrode ($-Q$ in the other electrode), and V is the voltage between the electrodes. The displacement W of any point x of the structure at time t can be expressed as a modal summation [6], relying on the modal coordinates q_i (with $i = 1, \dots, N$ where N is the number of modes considered and theoretically $N \to \infty$), and the eigenmodes Φ_i (scaled to the unit modal mass) of the structure with the piezoelectric patch in short-circuit, thus with V=0. The modal coordinates are the solutions of the following problem:

$$\ddot{q}_i + 2\xi_i\omega_i\dot{q}_i + \omega_i^2 q_i - \chi_i V = F_i \qquad \forall\, i \in \{1, \dots, N\} \tag{1}$$

$$C_\infty V - Q + \sum_{i=1}^{N} \chi_i q_i = 0 \tag{2}$$

where ω_i is the i^{th} eigenfrequency of the electro-mechanical system short-circuited, ξ_i is the associated non-dimensional damping ratio, and F_i is the modal force. Moreover, χ_i is a modal coupling coefficient that

describes the energy transfer between the piezoelectric patch and the i^{th} mode. Equation (1) describes the equations of motion of the system. The term χ_i couples these N equations of motion to Eq. (2) which models the electric behaviour of the electro-mechanical system. The symbols $\ddot{q}_i$ and $\dot{q}_i$ represent the second and first derivative of q_i with respect to the time, respectively. Finally, C_∞ is the electrical capacitance of the piezoelectric patch with blocked structure, which also corresponds to the value of the capacitance at infinite frequency. Moreover, V and $\dot{Q}$ (i.e. the derivative of Q with respect to the time, which is a current) are linked through Z_{sh} (see Figure 1) and, thus, this relation depends on the shunt circuit type. This link constitutes a further equation in addition to Eqs. (1) and (2).

The charge produced by the deflection of the piezoelectric actuator $\sum_{i=1}^{N} \chi_i q_i$ in Eq. (2) will be indicated as Q_{cs} (i.e. $Q_{\mathrm{cs}} = \sum_{i=1}^{N} \chi_i q_i$) for the sake of conciseness.

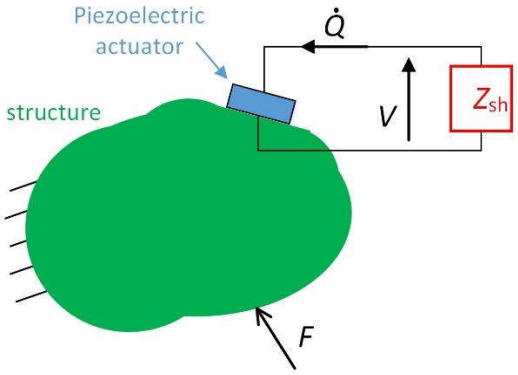

Figure 1: A generic forced structure with a piezoelectric patch shunted with an electric impedance Z_{sh}.

When Z_{sh} is made from an NC and a resistance R, two layouts can be used for the electric connection: parallel and series (see Figure 2, where V_{sh} and Q_{sh} are the voltage and charge seen by the resistance R, respectively. Here, -C_1 denotes the NC in the parallel layout, while -C_2 indicates the NC in the series layout). The series layout is usually used to mitigate low-order modes, while the parallel connection is employed to control high-order modes [49]. More details about this point will be given further in this section.

If a single-degree-of-freedom (SDOF) approximation is considered (which is valid in case of low modal density), the equations describing the electro-mechanical system for $\Omega \simeq \omega_i$ (where Ω is the angular frequency) have to be modified as explained in [49] in order to take into account the electrical contribution of the neglected modes. Particularly, the SDOF approximation requires to define a new capacitance value $C_{\mathrm{p}i}$ for the piezoelectric actuator. This new capacitance value is the sum of C_∞ and a capacitive term (C_i') which describes the residual contribution of the modes higher than the i^{th} (which are now not considered in the modal sum of Eq. (2)) in the frequency range of the i^{th} mode (see [49] for more details). Thus, the term C_∞ of Eq. (2) must be replaced with $C_{\mathrm{p}i} = C_\infty + C_i'$ when a reduced order model is considered. The influence of the lower modes is not considered because it is usually negligible (e.g. [15,57]).

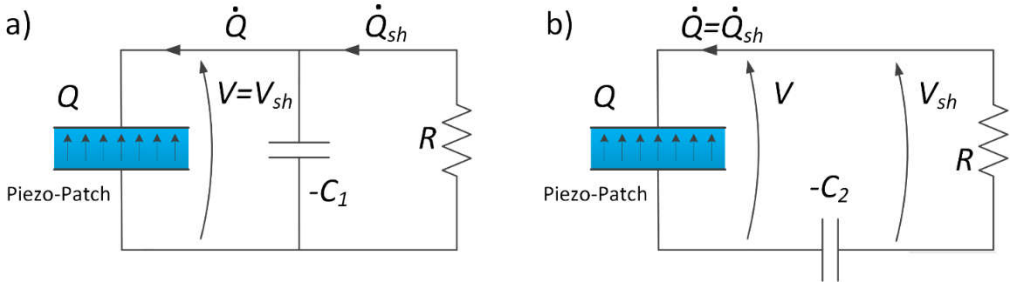

Figure 2: Parallel (a) and series (b) connection of the shunt impedance made from an NC and a resistance.

The term $C_{\mathrm{p}i}$, referred to as modal capacitance, can be found by measuring the value of the capacitance of the piezoelectric actuator midway between ω_i and ω_{i+1}. More details about its accurate estimation can be found in [42,58].

Furthermore, for the SDOF approximation around the i^{th} mode, the charge produced by the deflection of the piezoelectric actuator Q_{cs} is equal to $\chi_i q_i$ because a single mode is taken into account and the contribution of the higher modes is represented by the contribution C_i' in the $C_{\mathrm{p}i}$ term.

It is worth recalling that the previously mentioned modal electro-mechanical coupling factor k_i (see Section 1) is a normalized version of the term χ_i in Eq. (2) (i.e. $k_i = \chi_i/(\omega_i\sqrt{C_{\mathrm{p}i}})$, see [49]) and it can be also estimated by means of the values of the open- and short-circuit eigenfrequencies of the electro-mechanical system because it is close to the i^{th} effective coupling factor k_{eff} [6] (see [49] or Section 7.1).

According to the schematics of Figure 2, it is possible to write the relation between the current and the voltage seen by the shunt resistance *R*:

$$V_{\mathrm{sh}} = -R\dot{Q}_{\mathrm{sh}} \tag{3}$$

Relying on the normalized parameters $\bar{V}_{\mathrm{sh}}$ and $\bar{Q}_{\mathrm{sh}}$, it is possible to write the equations describing the dynamics of the SDOF system [49]:

$$\ddot{q}_i + 2\xi_i\omega_i\dot{q}_i + (\omega_i^{\mathrm{oc}})^2 q_i - \omega_i\tilde{k}_i\bar{Q}_{\mathrm{sh}} = F_i \tag{4}$$

$$\bar{V}_{\mathrm{sh}} - \bar{Q}_{\mathrm{sh}} + \omega_i\tilde{k}_i q_i = 0 \tag{5}$$

where $\bar{V}_{\mathrm{sh}} = V_{\mathrm{sh}}\sqrt{C_{\mathrm{eq}}}$ and $\bar{Q}_{\mathrm{sh}} = Q_{\mathrm{sh}}/\sqrt{C_{\mathrm{eq}}}$.

The parameter C_{eq} is an equivalent capacitance that includes the effect of the NC and whose expression depends on the NC layout (parallel or series, see Figure 2), on the value of the NC and on $C_{\mathrm{p}i}$ (see Table 1). The symbol ω_i^{oc} represents the eigenfrequency of the electro-mechanical system when *R* is an open-circuit (i.e. Q_{sh}=0). It is also possible to define ω_i^{sc} (which is used further in the paper) that is the eigenfrequency of the electro-mechanical system when *R* is a short-circuit (i.e. V_{sh}=0). Also the expressions of these eigenfrequencies can be found in Table 1 and they are functions of k_i.

Table 1: Definition of C_{eq}, ω_i^{sc}, ω_i^{oc} and $\widetilde{k}_i$ [49]**.**

	NC in parallel	NC in series
C_{eq}=	$C_{\mathrm{p}i}$-C_1	$\dfrac{C_2 C_{\mathrm{p}i}}{C_2 - C_{\mathrm{p}i}}$
ω_i^{sc}=	ω_i	$\omega_i\sqrt{1 - \dfrac{(C_{\mathrm{p}i}/C_2)k_i^2}{1-(C_{\mathrm{p}i}/C_2)}}$
ω_i^{oc}=	$\omega_i\sqrt{1 + \dfrac{k_i^2}{1-(C_1/C_{\mathrm{p}i})}}$	$\omega_i\sqrt{1+k_i^2}$
$\tilde{k}_i$=	$\dfrac{k_i}{\sqrt{1-(C_1/C_{\mathrm{p}i})}}$	$\dfrac{k_i}{\sqrt{1-(C_{\mathrm{p}i}/C_2)}}$

Finally, the term $\tilde{k}_i$ in Eqs. (4) and (5) is the enhanced modal electro-mechanical coupling factor and it assumes the expressions gathered in Table 1. The analytical expression of $\tilde{k}_i$ depends on the value of k_i of the system (without NCs), and on the layout used to connect the NCs, whose effect is to increase the initial value of $|k_i|$. As mentioned, when no NCs are used, the level of vibration reduction depends on the value of $|k_i|$ that is a parameter indicating the efficiency of the electro-mechanical energy conversion. The higher $|k_i|$ is, the higher the maximum achievable attenuation performance is [6]. $|\tilde{k}_i|$ expresses the increase of $|k_i|$ thanks to the use of NCs (i.e. $|\tilde{k}_i| \geq |k_i|$) and, therefore, this increase turns into higher attenuation levels provided by the piezoelectric shunt [49].

The model described by Eqs. (1) to (5) is a modal model. Therefore, it is of general validity, regardless the type of structure considered and can be applied to both simple and complex structures. Moreover, Eqs. (1) to (5) are general and valid for both the NC connections shown in Figure 2. However, the values of the NC must respect specific stability conditions. Indeed, since the NC has an active nature, instability can arise. According to [49], the stability conditions are $C_1 < C_\infty$ for the NC in parallel connection and $C_2 > C_0$ for the NC in series connection, where C_0 is the value of the capacitance of the piezoelectric actuator bonded to the structure at the null frequency. In all the analyses, examples and experiments discussed further in this paper, the value of the NC is always chosen such that the previous stability conditions are fulfilled.

A last remark is related to a point already evidenced in this section: the series NC is usually used to mitigate low-order modes, while the parallel connection is employed to control high-order modes. It was demonstrated in [49] that the attenuation improvement on a given mode accomplished by means of an NC increases when the value of either C_1 or C_2 approaches the $C_{\mathrm{p}i}$ value of the mode considered. According to the stability limits and to the fact that $C_0 > C_{\mathrm{p}i} > C_{\mathrm{p}(i+1)} > C_\infty$ [49], C_2 (NC in series), being greater than C_0, can be closer to $C_{\mathrm{p}i}$ than C_1 (that is lower than C_∞) (NC in parallel) for low order modes. Conversely, for high-order modes, C_1 (NC in parallel) can be closer to $C_{\mathrm{p}i}$ than C_2 (NC in series). This is the reason why NCs in series are used to control low-order modes and NCs in parallel for high-order modes. Depending on the system considered, the mode number for which an NC in series can become advantageous compared to an NC in parallel can change according to the values of $C_{\mathrm{p}i}$ for the different modes and the stability thresholds C_0 and C_∞. Generally speaking, it is possible to roughly conclude that NCs in series are usually used for modes up to few kilohertz, while NCs in parallel are used at higher frequency values.

The model expressed by Eqs. (1) and (2) is of general validity. Conversely, Eqs. (4) and (5) are related to an SDOF approximation of the system. In this paper, the authors will first use the general model (Eqs. (1) and (2)). However, in Section 4.1, they will also employ the SDOF model to derive conclusions which will be then extended to MDOF systems in Section 4.2. Indeed, it will be shown that the use of an SDOF approximation easily allows to express normalized parameters and improves the clarity of the whole discussion without leading to any loss of generality.

2.2 NC electrical circuits

As mentioned previously, NCs are built using circuits based on OP-AMPs. In this work, an ideal behavior of the OP-AMP will be considered [50]. Depending on the connection between the piezoelectric transducer and the NC, different circuits can be used. When the NC is connected in parallel (see Figure 2a), two schematics can be employed, named type A and B, which differ from each other for the capacitance position in the circuit. They are shown in Figure 3a (named layout PA, where P indicates the parallel connection) and Figure 3b (named layout PB). Both the layouts provide an equivalent circuit which is a pure NC, -C_1, whose value can be calculated as:

$$C_1 = \frac{R_2}{R_1}\hat{C} \tag{6}$$

Since the obtained equivalent circuit is the same for both the layouts (i.e. -C_1), also the attenuation performance provided by the two layouts will be the same.

When the NC is connected in series (see Figure 2b), there are again two different possible layouts that can be used and they are the type A and B of Figure 3a and Figure 3b with the OP-AMP pins exchanged. However, often, problems are encountered with these layouts [59], caused for example by bias currents, and thus different layouts are used in practical applications: layouts SA (see Figure 3c) and SB (see Figure 3d). It is worth noticing that in this case there are two additional elements compared to the parallel layouts: the resistances R_s and $\hat{R}$. The resistance $\hat{R}$ is added to avoid electrical problems [59] but its presence also causes a destabilizing effect [60], which is limited by the addition of R_s [49]. The circuits SA and SB can be seen as the parallel between an NC, -C_2, and a resistance R_{eq}, where:

$$C_2 = \frac{R_2}{R_1}\hat{C} \tag{7}$$

$$R_{eq} = \frac{R_s \frac{R_1}{R_2}\hat{R}}{\frac{R_1}{R_2}\hat{R} - R_s} \tag{8}$$

The value of R_s is usually chosen in order to make R_{eq} tend to $-\infty$ (e.g. -75 MΩ). This allows to make the SA and SB layouts behave similarly to pure NCs (with the exception of the low frequency range, e.g. below 10 Hz, which is usually not interesting for piezoelectric shunt applications). Therefore, these layouts will be considered as ideal from here on (i.e. considering just R_1, R_2 and $\hat{C}$ to model the electrical behaviour of the NC and neglecting R_s and $\hat{R}$).

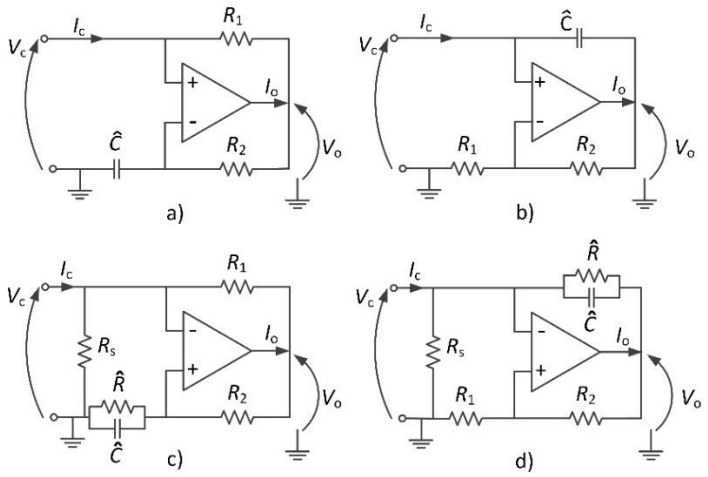

Figure 3: Physical implementation of NCs: type PA (a), type PB (b), type SA (c) and type SB (d).

Once recalled the electro-mechanical system model and the NC schematics and layouts, it is possible to approach the problem of OP-AMP outputs, which is the main focus of this work.

2.3 The outputs of the OP-AMP

In this subsection the general model described by Eqs. (1) and (2) is employed to derive the model describing the behaviour of the OP-AMP in terms of its output voltage and current. Particularly, the frequency response functions (FRFs) $G(\mathrm{j}\Omega)$ between the charge Q_{cs} produced by the deflection of the piezoelectric actuator ($Q_{\mathrm{cs}} = \sum_{i=1}^{N} \chi_i q_i$, see Eq. (2)) and either the voltage V_{o} or the current I_{o} at the output of the OP-AMP (see Figure 3) are derived. These FRFs will constitute the basis for all the subsequent analyses and, since they are based on Eq. (2), they are of general validity.

According to Eq.(2), Figure 2 and Figure 3, and the link between V and $\dot{Q}$ through Z_{sh} (see Figure 1), it is possible to derive the FRFs $G(\mathrm{j}\Omega)$:

$$G_{\mathrm{pa}}^{\mathrm{vo}}(\mathrm{j}\Omega) = \frac{V_{\mathrm{o}}}{Q_{\mathrm{cs}}}(\mathrm{j}\Omega) = \frac{1 + \mathrm{j}\Omega C_1 R_1}{(C_1 - C_\infty) - 1/(\mathrm{j}\Omega R)}\,, \qquad G_{\mathrm{pa}}^{\mathrm{io}}(\mathrm{j}\Omega) = \frac{I_{\mathrm{o}}}{Q_{\mathrm{cs}}}(\mathrm{j}\Omega) = \frac{\mathrm{j}\Omega C_1[1 + (R_1/R_2)]}{(C_1 - C_\infty) - 1/(\mathrm{j}\Omega R)} \tag{9}$$

$$G_{\mathrm{pb}}^{\mathrm{vo}}(\mathrm{j}\Omega) = \frac{V_{\mathrm{o}}}{Q_{\mathrm{cs}}}(\mathrm{j}\Omega) = \frac{1 + (R_2/R_1)}{(C_1 - C_\infty) - 1/(\mathrm{j}\Omega R)}\,, \qquad G_{\mathrm{pb}}^{\mathrm{io}}(\mathrm{j}\Omega) = \frac{I_{\mathrm{o}}}{Q_{\mathrm{cs}}}(\mathrm{j}\Omega) = \frac{\mathrm{j}\Omega C_1 + (1/R_1)}{(C_1 - C_\infty) - 1/(\mathrm{j}\Omega R)} \tag{10}$$

$$G_{\mathrm{sa}}^{\mathrm{vo}}(\mathrm{j}\Omega) = \frac{V_{\mathrm{o}}}{Q_{\mathrm{cs}}}(\mathrm{j}\Omega) = \frac{1 + \mathrm{j}\Omega C_2 R_1}{(C_2 - C_\infty) + \mathrm{j}\Omega R C_2 C_\infty}\,, \qquad G_{\mathrm{sa}}^{\mathrm{io}}(\mathrm{j}\Omega) = \frac{I_{\mathrm{o}}}{Q_{\mathrm{cs}}}(\mathrm{j}\Omega) = \frac{\mathrm{j}\Omega C_2[1 + (R_1/R_2)]}{(C_2 - C_\infty) + \mathrm{j}\Omega R C_2 C_\infty} \tag{11}$$

$$G_{\mathrm{sb}}^{\mathrm{vo}}(\mathrm{j}\Omega) = \frac{V_{\mathrm{o}}}{Q_{\mathrm{cs}}}(\mathrm{j}\Omega) = \frac{1 + (R_2/R_1)}{(C_2 - C_\infty) + \mathrm{j}\Omega R C_2 C_\infty}\,, \qquad G_{\mathrm{sb}}^{\mathrm{io}}(\mathrm{j}\Omega) = \frac{I_{\mathrm{o}}}{Q_{\mathrm{cs}}}(\mathrm{j}\Omega) = \frac{\mathrm{j}\Omega C_2 + (1/R_1)}{(C_2 - C_\infty) + \mathrm{j}\Omega R C_2 C_\infty} \tag{12}$$

The superscripts vo and io indicate voltage and current OP-AMP outputs, respectively. The subscript, instead, indicates the configuration used (i.e. p for parallel and s for series, and a for type A and b for type B).

From these FRFs, their corresponding absolute values $M(\Omega)$ can be derived:

$$M_{\mathrm{pa}}^{\mathrm{vo}}(\Omega) = |G_{\mathrm{pa}}^{\mathrm{vo}}(\mathrm{j}\Omega)| = \frac{\sqrt{1 + (\Omega C_1 R_1)^2}}{P_{\mathrm{M}}}\,, \qquad M_{\mathrm{pa}}^{\mathrm{io}}(\Omega) = |G_{\mathrm{pa}}^{\mathrm{io}}(\mathrm{j}\Omega)| = \frac{\Omega C_1[1 + (R_1/R_2)]}{P_{\mathrm{M}}} \tag{13}$$

$$M_{\mathrm{pb}}^{\mathrm{vo}}(\Omega) = |G_{\mathrm{pb}}^{\mathrm{vo}}(\mathrm{j}\Omega)| = \frac{1 + (R_2/R_1)}{P_{\mathrm{M}}}\,, \qquad M_{\mathrm{pb}}^{\mathrm{io}}(\Omega) = |G_{\mathrm{pb}}^{\mathrm{io}}(\mathrm{j}\Omega)| = \frac{\sqrt{(\Omega C_1)^2 + (1/R_1)^2}}{P_{\mathrm{M}}} \tag{14}$$

$$M_{\mathrm{sa}}^{\mathrm{vo}}(\Omega) = |G_{\mathrm{sa}}^{\mathrm{vo}}(\mathrm{j}\Omega)| = \frac{\sqrt{1 + (\Omega C_2 R_1)^2}}{S_{\mathrm{M}}}\,, \qquad M_{\mathrm{sa}}^{\mathrm{io}}(\Omega) = |G_{\mathrm{sa}}^{\mathrm{io}}(\mathrm{j}\Omega)| = \frac{\Omega C_2[1 + (R_1/R_2)]}{S_{\mathrm{M}}} \tag{15}$$

$$M_{\mathrm{sb}}^{\mathrm{vo}}(\Omega) = |G_{\mathrm{sb}}^{\mathrm{vo}}(\mathrm{j}\Omega)| = \frac{1 + (R_2/R_1)}{S_{\mathrm{M}}}\,, \qquad M_{\mathrm{sb}}^{\mathrm{io}}(\Omega) = |G_{\mathrm{sb}}^{\mathrm{io}}(\mathrm{j}\Omega)| = \frac{\sqrt{(\Omega C_2)^2 + (1/R_1)^2}}{S_{\mathrm{M}}} \tag{16}$$

where:

$$P_{\mathrm{M}} = \sqrt{(C_1 - C_\infty)^2 + 1/(\Omega R)^2}\,, \qquad S_{\mathrm{M}} = \sqrt{(C_2 - C_\infty)^2 + (\Omega R C_2 C_\infty)^2} \tag{17}$$

In the next section, the formulations in Eqs. (9) to (17) will be used to show that it is possible to decrease the OP-AMP output without changing the attenuation performance, as well as to compare NC circuits A and B. Considering the series and parallel connections of the NCs, as mentioned in Section 2.1, the series layout is used to damp low-order modes, while the parallel connection is employed to control high-order modes. Therefore, no comparisons will be addressed between series and parallel connections because of their different use.

3 The change of the OP-AMP outputs without changing the attenuation performance

According to Berardengo et al. [49], the attenuation performance is fixed as soon as the value of the NC (i.e. $-C_1$ or $-C_2$) and the value of the shunt resistance R are set. Therefore, in order to see whether it is possible to change the OP-AMP outputs without changing the performance of the control, the trend of the M^{vo} and M^{io} functions must be analysed keeping fixed the values of C_1, C_2 and R, which are thus treated as constants in this analysis.

In this case, a change of the OP-AMP outputs can be thus obtained by changing either R_1 or R_1/R_2, which are the only free parameters. Obviously, any change of R_1 and R_1/R_2 must be compensated in Eqs. (6) and (7) in order to maintain the value of the NC constant. As an example, if $M_{\mathrm{pa}}^{\mathrm{io}}$ is considered (Eq. (13)), when R_1/R_2 is changed, the value of $\hat{C}$ (see Eq. (6)) must be changed accordingly in order to maintain the value of -C_1 constant.

Table 2 indicates the effect of R_1 and R_1/R_2 on V_o and I_o for the different circuit configurations of the NC (type A and B) and is valid for an NC in both parallel and series connection. As an example, if the configuration SA is used, and the aim is to decrease the value of V_o, the value of R_1 must be decreased (see Eq. (15)). From Table 2, it is evident that inverse behaviours characterise types A and B NCs: high values of R_1 and R_1/R_2 are favorable for type B, while low values are fine for type A. However, it must be underlined that the values of R_1 and R_1/R_2 cannot be indefinitely decreased/increased because this could cause problems to the electrical part of the electro-mechanical system. The limit values for R_1 and R_1/R_2 must be looked for case by case because they depend on the non-ideal behavior of the OP-AMP.

Even if most of the times the OP-AMP saturation is related to the output voltage, also the behaviour in terms of current output has been included in this analysis. It is worth noticing that, for each configuration, it is possible to act separately on V_o and I_o because, when one depends on R_1, the other one depends on R_1/R_2. This is an important outcome because it evidences that it is possible to decrease the electrical power required from the OP-AMP. If applications where there is a limited availability of electrical power are considered, this aspect can become fundamental for the practical application of the NC.

Table 2: Effect of R_1 and R_1/R_2 on the OP-AMP outputs for an NC in either parallel or series connection

	Type A		Type B	
	$M_{\mathrm{a}}^{\mathrm{vo}}$	$M_{\mathrm{a}}^{\mathrm{io}}$	$M_{\mathrm{b}}^{\mathrm{vo}}$	$M_{\mathrm{b}}^{\mathrm{io}}$
If R_1 increases and R_1/R_2 does not change	increases	no change	no change	decreases
If R_1/R_2 increases and R_1 does not change	no change	increases	decreases	no change

Figure 4 provides some quantitative examples of the relations among M^{vo}, M^{io} and either R_1 or R_1/R_2 expressed in Table 2 (obviously, where there is no dependence between two quantities, the plot is not shown, e.g. the trend of $M_{\mathrm{a}}^{\mathrm{vo}}(\Omega)$ as a function of R_1/R_2 is not shown because it is not a function of R_1/R_2). This figure shows the amount of change of V_{o} and I_{o} (considering the amplitudes M, see Eqs. (13) to (16)) that can be obtained changing the values of R_1 and R_1/R_2. The results of Figure 4 are valid for NCs in both parallel and series connection. The values on the vertical axes of Figure 4 are normalized (as indicated by the word 'norm' in the superscript) in order to have a value equal to 1 for the highest value of each curve and a straightforward percentage comparison. The plots show that a significant decrease of the output current and voltage can be achieved acting on the circuit parameters for both type A and B NCs. As an example, Figure 4a shows that, once the value of the NC is set, a decrease of R_1 from 25 kΩ to 6 kΩ allows to decrease the output voltage for type A of about 15% or much more (this result is a function of the frequency value considered; Figure 4a shows the curves for three different values of Ω) (see Eqs. (13) and (15)). In Figure 4b, it is shown that the output voltage for type B can be decreased of about a half increasing the value of R_1/R_2 from 0.5 to 1.5 and this result is not dependent on the frequency (see Eqs. (14) and (16)).

Looking at Eq. (17), it is interesting to notice that the changes of R_1 and R_1/R_2 do not affect the denominator of the M functions (see Eqs. (13) to (16)). Moreover, the denominator of these functions is always the same for a given NC connection (series or parallel). This peculiarity allows for a straightforward comparison of the A and B circuits in terms of both voltage and current output, by calculating the ratios D:

$$D_{\mathrm{p}}^{\mathrm{vo}}(\Omega) = \frac{M_{\mathrm{pa}}^{\mathrm{vo}}(\Omega)}{M_{\mathrm{pb}}^{\mathrm{vo}}(\Omega)} = D_{\mathrm{s}}^{\mathrm{vo}}(\Omega) = \frac{M_{\mathrm{sa}}^{\mathrm{vo}}(\Omega)}{M_{\mathrm{sb}}^{\mathrm{vo}}(\Omega)} = \frac{\sqrt{1 + (\Omega C_{\mathrm{neg}} R_1)^2}}{1 + (R_2/R_1)} \tag{18}$$

$$D_{\mathrm{p}}^{\mathrm{io}}(\Omega) = \frac{M_{\mathrm{pa}}^{\mathrm{io}}(\Omega)}{M_{\mathrm{pb}}^{\mathrm{io}}(\Omega)} = D_{\mathrm{s}}^{\mathrm{io}}(\Omega) = \frac{M_{\mathrm{sa}}^{\mathrm{io}}(\Omega)}{M_{\mathrm{sb}}^{\mathrm{io}}(\Omega)} = \frac{\Omega C_{\mathrm{neg}}[1 + (R_1/R_2)]}{\sqrt{(\Omega C_{\mathrm{neg}})^2 + (1/R_1)^2}} \tag{19}$$

where $C_{\mathrm{neg}} = C_1$ for an NC in parallel and $C_{\mathrm{neg}} = C_2$ for an NC in series.

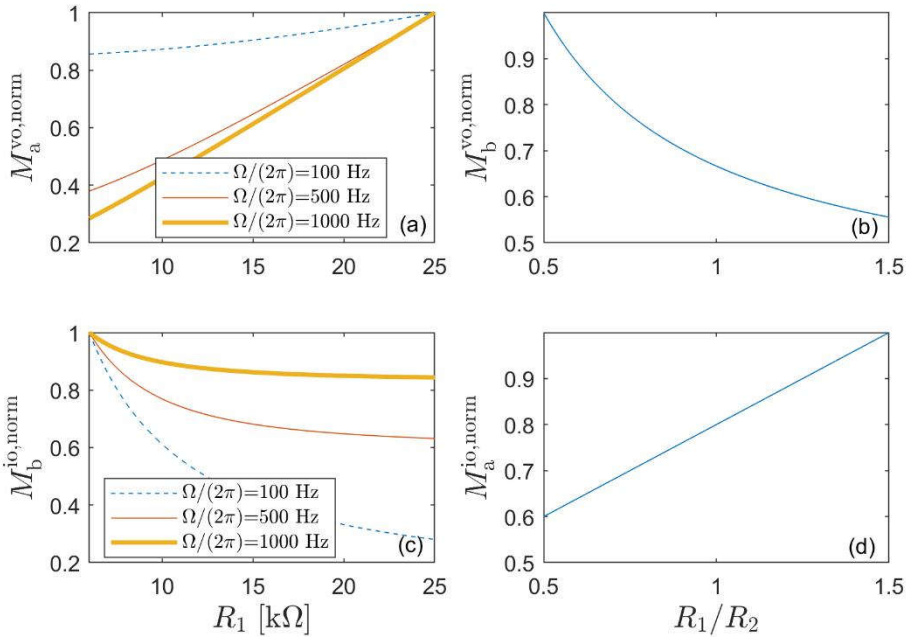

Figure 4: Trend of M^{vo} and M^{io} as a function of R_1 and R_1/R_2 (valid for both series and parallel NC). The values on the vertical axes are normalized (as indicated by the word 'norm' in the superscript) in order to have a value equal to 1 for the highest value of each curve. $M_{\mathrm{a}}^{\mathrm{vo,norm}}$ (a), $M_{\mathrm{b}}^{\mathrm{vo,norm}}$ (b), $M_{\mathrm{b}}^{\mathrm{io,norm}}$ (c) and $M_{\mathrm{a}}^{\mathrm{io,norm}}$ (d). The absolute value of the NC is 40 nF.

In order to show a comparison between the two types of NC circuits (A and B), Figure 5 shows the trend of D^{vo} and D^{io} as a function of the frequency for a system chosen as an example, where the values of R_1 and R_1/R_2 have been set to values that are common in practical cases (low value of R_1, i.e. 6 kΩ, which is fine for type A and high value of R_1/R_2, i.e. 1.5, which is fine for type B). The plots of Figure 5 are valid for an NC in both parallel and series connection. Figure 5 and Eqs. (18) and (19) show that these ratios are function of the angular frequency Ω. This means that, depending on the frequency band considered (and also on the value of NC used), type A NC can be either better or worse (in terms of level of output) than type B. As an example, Figure 5a shows that a frequency value exists over which D^{vo} becomes higher than 1, which means that type B becomes less demanding than type A. This threshold frequency value depends on the value of the NC used. It is also noticed that the ratios D do not depend on the value of R. In the case presented in Figure 5a with an NC equal to 40 nF, type A must be preferred if the response of the structure is concentrated below about 1 kHz, while type B must be preferred if it is concentrated over approximately 1 kHz. In case the response is not concentrated in one of these two frequency bands, a multi-mode approach becomes essential to choose the right configuration between types A and B.

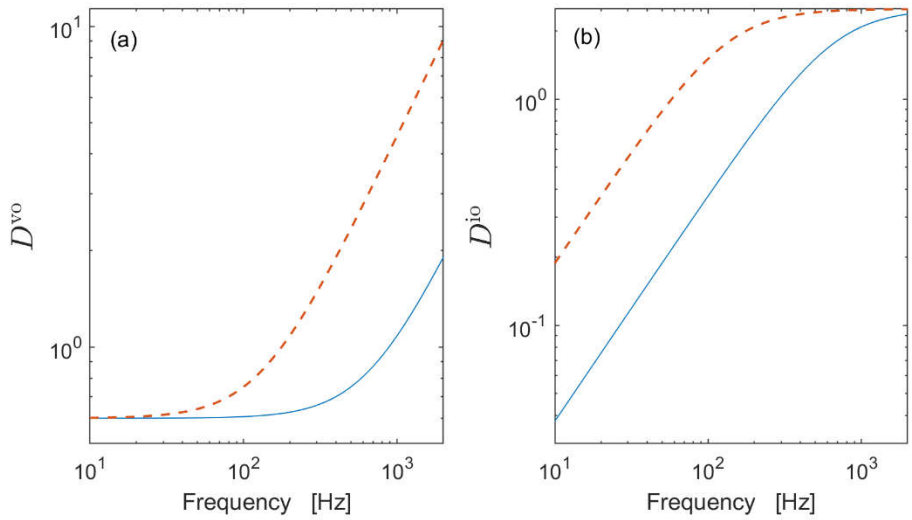

Figure 5: Trend D^{vo} (a) and D^{io} (b) (valid for both series and parallel NC connections) as a function of the frequency for an NC absolute value equal to 40 nF (solid line) and 200 nF (dashed line), $R_1 = 6\ \mathrm{k\Omega}$ and $R_1/R_2 = 1.5$.

Therefore, for a given engineering application, an MDOF model must be used in order to understand which is the most convenient NC circuit (A or B). This problem will be addressed in detail in Sections 5 and 6.

The analysis presented in this section has shown that it is possible to decrease the OP-AMP output without changing the attenuation performance by properly tuning the values of R_1 and R_1/R_2. Furthermore, nor type A circuit neither type B circuit can be considered better than the other because of the relation between the OP-AMP outputs and the frequency, that makes one type more/less demanding than the other according to the frequency range considered.

In case a generic passive impedance *Z* is used in place of a simple resistance *R* in Figure 2, the FRFs of Eqs. (9) to (12) can be changed by simply replacing the value of *R* at the denominator with the expression of the generic passive impedance *Z*. Being *Z* always at the denominator of the FRFs, the results of this section can be readily shown to be valid for any type of passive impedance (moreover, it must be noticed that Eqs. (18) and (19) do not change). Particularly, the trend of the current and the voltage at the OP-AMP outputs do not change and the conclusions outlined in Table 2, Figure 4 and Figure 5 become of general validity, regardless the type of passive impedance used in Figure 2 in place of the resistance *R*.

4 The effect of the NC and *R* values on the OP-AMP outputs

In section 3, attention was focused on how to change the OP-AMP outputs, given a certain attenuation performance. However, it is worth analysing also what occurs if this constraint is removed and, thus, studying the effect of the values of the NC and *R* on the OP-AMP voltage and current outputs. Indeed, this will allow to understand also how the vibration level of the electro-mechanical system affects the OP-AMP outputs.

As an example, suppose to change the value of *R*. On the one hand, this change causes a change of the OP-AMP output due to the electric behavior of the shunt impedance, as can be noticed looking at Eqs. (13) to (16) which link the value of *R* to the OP-AMP outputs. However, a second effect occurs because the change of *R* also changes the vibration of the electro-mechanical system [49]. If the vibration increases/decreases, the value of Q_{cs} ($Q_{cs} = \sum_{i=1}^{N} \chi_i q_i$, see Eq. (2)) increases/decreases and, therefore, a change of the OP-AMP output occurs.

The aforementioned facts suggest that, for a detailed analysis of the effect of the NC and *R* values on the OP-AMP outputs, it is not enough to consider just the electrical part of the electro-mechanical system. Therefore, this paper considers the whole electro-mechanical system (i.e. also the mechanical part).

This paper proposes to address the mentioned points by deriving the FRFs between the external forcing term *F* and the OP-AMP outputs. In this section, this is accomplished by considering at first (Section 4.1) the SDOF approximation of the whole system described in section 2.1 because it offers a clear view of the phenomena involved in the problem, without any loss of generality. The results of the discussion related to the SDOF system are then generalized to a generic MDOF system in Section 4.2.

4.1 SDOF system

To the purpose of this section, it is convenient to use the non-dimensional parameters k_i, $\tilde{k}_i$ and τ in place of the physical parameters (i.e. $-C_1$, $-C_2$ and R) to express Eqs. (9) to (12) which describe the FRFs $G(\mathrm{j}\Omega)$ between the charge Q_{cs} ($Q_{\mathrm{cs}} = \chi_i q_i$ for the SDOF approximation, see Section 2.1) produced by the deflection of the piezoelectric transducer and either the voltage V_{o} or the current I_{o} at the output of the OP-AMP. The parameter τ is defined as:

$$\tau = C_{\mathrm{eq}} R \tag{20}$$

The use of the parameters k_i, $\tilde{k}_i$ and τ in the FRFs $G(\mathrm{j}\Omega)$ allows to readily link the electrical behavior of the electro-mechanical system to the mechanical one. Indeed, the values of $\tilde{k}_i$, k_i and τ are directly related to the vibration attenuation provided by the piezoelectric shunt and, thus, allow to study the OP-AMP outputs as functions also of the control performance.

According to Eq. (20) and to the expressions of C_{eq} and $\tilde{k}_i$ given Table 1, the FRFs of Eqs. (9) to (12) can be expressed for an SDOF system as:

$$G^{\mathrm{vo}}_{i,\mathrm{pa}}(\mathrm{j}\Omega) = \frac{V_{\mathrm{o}}}{Q_{\mathrm{cs}}}(\mathrm{j}\Omega) = \frac{\tilde{k}_i^2 + \mathrm{j}\Omega C_{\mathrm{p}i}(\tilde{k}_i^2 - k_i^2)R_1}{P_i \tilde{k}_i^2}\,, G^{\mathrm{io}}_{i,\mathrm{pa}}(\mathrm{j}\Omega) = \frac{I_{\mathrm{o}}}{Q_{\mathrm{cs}}}(\mathrm{j}\Omega) = \frac{\mathrm{j}\Omega C_{\mathrm{p}i}(\tilde{k}_i^2 - k_i^2)[1 + (R_1/R_2)]}{P_i \tilde{k}_i^2} \tag{21}$$

$$G^{\mathrm{vo}}_{i,\mathrm{pb}}(\mathrm{j}\Omega) = \frac{V_{\mathrm{o}}}{Q_{\mathrm{cs}}}(\mathrm{j}\Omega) = \frac{1 + (R_2/R_1)}{P_i}\,, \qquad G^{\mathrm{io}}_{i,\mathrm{pb}}(\mathrm{j}\Omega) = \frac{I_{\mathrm{o}}}{Q_{\mathrm{cs}}}(\mathrm{j}\Omega) = \frac{\mathrm{j}\Omega C_{\mathrm{p}i}(\tilde{k}_i^2 - k_i^2) + \tilde{k}_i^2(1/R_1)}{P_i \tilde{k}_i^2} \tag{22}$$

$$G^{\mathrm{vo}}_{i,\mathrm{sa}}(\mathrm{j}\Omega) = \frac{V_{\mathrm{o}}}{Q_{\mathrm{cs}}}(\mathrm{j}\Omega) = \frac{(\tilde{k}_i^2 - k_i^2) + \mathrm{j}\Omega C_{\mathrm{p}i}\tilde{k}_i^2 R_1}{S_i(\tilde{k}_i^2 - k_i^2)}\,, \qquad G^{\mathrm{io}}_{i,\mathrm{sa}}(\mathrm{j}\Omega) = \frac{I_{\mathrm{o}}}{Q_{\mathrm{cs}}}(\mathrm{j}\Omega) = \frac{\mathrm{j}\Omega C_{\mathrm{p}i}\tilde{k}_i^2[1 + (R_1/R_2)]}{S_i(\tilde{k}_i^2 - k_i^2)} \tag{23}$$

$$G^{\mathrm{vo}}_{i,\mathrm{sb}}(\mathrm{j}\Omega) = \frac{V_{\mathrm{o}}}{Q_{\mathrm{cs}}}(\mathrm{j}\Omega) = \frac{1 + (R_2/R_1)}{S_i}\,, \qquad G^{\mathrm{io}}_{i,\mathrm{sb}}(\mathrm{j}\Omega) = \frac{I_{\mathrm{o}}}{Q_{\mathrm{cs}}}(\mathrm{j}\Omega) = \frac{\mathrm{j}\Omega C_{\mathrm{p}i}\tilde{k}_i^2 + (1/R_1)(\tilde{k}_i^2 - k_i^2)}{S_i(\tilde{k}_i^2 - k_i^2)} \tag{24}$$

where the subscript i is added to G to indicate the mode considered, and:

$$P_i = -C_{\mathrm{p}i}\frac{(1+\mathrm{j}\Omega\tau)k_i^2}{\mathrm{j}\Omega\tau\tilde{k}_i^2}\,, \qquad S_i = C_{\mathrm{p}i}(1+\mathrm{j}\Omega\tau)\frac{k_i^2}{\tilde{k}_i^2-k_i^2} \tag{25}$$

Furthermore, according to [49], the FRF H_i between the modal force F_i and the modal coordinate q_i is:

$$H_i(\mathrm{j}\Omega) = \frac{q_i}{F_i}(\mathrm{j}\Omega) = \frac{1+\mathrm{j}\Omega\tau}{\left(\omega_i^{\mathrm{sc}}\right)^2-(1+2\xi_i\omega_i\tau)\Omega^2+\mathrm{j}\Omega\left[\tau\left(\omega_i^{\mathrm{oc}}\right)^2+2\xi_i\omega_i-\tau\Omega^2\right]} \tag{26}$$

Therefore, using Eqs. (21) to (24), together with Eq. (26), the FRFs T_i^{vo}, between the external force F and V_{o}, and T_i^{io}, between the external force F and I_{o}, can be derived for an SDOF system:

$$T_i^{\mathrm{vo}}(\mathrm{j}\Omega) = \frac{V_{\mathrm{o}}}{F}(\mathrm{j}\Omega) = \frac{V_{\mathrm{o}}}{Q_{\mathrm{cs}}}\chi_i\Phi_i(x_{\mathrm{f}})\frac{q_i}{F_i} = \chi_i\Phi_i(x_{\mathrm{f}})G_i^{\mathrm{vo}}(\mathrm{j}\Omega)H_i(\mathrm{j}\Omega) \tag{27}$$

$$T_i^{\mathrm{io}}(\mathrm{j}\Omega) = \frac{I_{\mathrm{o}}}{F}(\mathrm{j}\Omega) = \frac{I_{\mathrm{o}}}{Q_{\mathrm{cs}}}\chi_i\Phi_i(x_{\mathrm{f}})\frac{q_i}{F_i} = \chi_i\Phi_i(x_{\mathrm{f}})G_i^{\mathrm{io}}(\mathrm{j}\Omega)H_i(\mathrm{j}\Omega) \tag{28}$$

where x_{f} is the point where F acts on the mechanical structure.

If the amplitudes of the FRFs T_i^{vo} and T_i^{io} are considered, it is easy to notice that their peaks are at frequency values corresponding to (or very close to) the peak values of the amplitudes of the FRFs H_i.

Figure 6 shows, for two electro-mechanical systems chosen as examples, the trend of the peaks for the FRF amplitudes of T_i^{vo}, named T^{pk}, and of H_i, named H^{pk}, as functions of the value of τ (the value of τ is expressed in Figure 6 as normalised over its optimal value τ^{opt}, i.e. the value which maximises the vibration attenuation [49] for the mode considered). The value of τ is changed on the horizontal axis of the plot by changing the value of R, keeping always the same value for the NC and, thus, for the C_{eq} involved in the definition of τ (see Eq. (20) and Table 1). Moreover, the figure also shows the values of the G_i^{vo} amplitude at the frequency value where the FRFs T_i^{vo} have their amplitude peaks, named G^{pk}.

The trends of T^{pk}, H^{pk}, and G^{pk} as functions of the value of τ/τ^{opt} are shown in Figure 6 as normalized (as indicated by the superscript 'norm') in order to have 1 as maximum value for each curve, for a straightforward comparison of the trends. This representation allows to highlight the contribution to the output voltage (for a given value of the input force) of the electrical part of the system (represented by G^{pk}) and the mechanical one (represented by H^{pk}).

Figure 6 shows that when the value of τ is much higher than τ^{opt} ($\tau/\tau^{\mathrm{opt}} \geq 50$), the behavior of $T^{\mathrm{pk,norm}}$ is close to the behavior of $G^{\mathrm{pk,norm}}$, thus highly influenced by the electrical part of the whole system. Conversely, for $\tau/\tau^{\mathrm{opt}} \leq 5$, the behavior of $T^{\mathrm{pk,norm}}$ is significantly different from that of $G^{\mathrm{pk,norm}}$, while it stays close to that of $H^{\mathrm{pk,norm}}$. As an example, for τ/τ^{opt} from 0.01 to 0.1, the trend of $G^{\mathrm{pk,norm}}$ is almost constant. Conversely, $T^{\mathrm{pk,norm}}$ decreases, following the behaviour of $H^{\mathrm{pk,norm}}$ that decreases due to the reduction of the vibration provided by the shunt. The percentage decrease of $T^{\mathrm{pk,norm}}$ in the range of τ/τ^{opt} from 0.01 to 0.1 is significant (i.e. about 60% for plot (a) of Figure 6, and about 70% for plot (b)), evidencing that the behavior of the mechanical part of the electro-mechanical system has a significant influence on the OP-AMP outputs. This in turn demonstrates that it possible to decrease the OP-AMP outputs at resonance, when the value of the resistance R is optimized, thanks to the decrease of the

electro-mechanical system vibration. Therefore, it is not possible to analyse the effect of the value of *R* on the OP-AMP outputs taking into account just the electric part of the electro-mechanical system. It is worth noticing that, although Figure 6 is related to voltage output for type A circuit (NC in series), similar curve trends can be obtained when type B circuit and/or current output are considered.

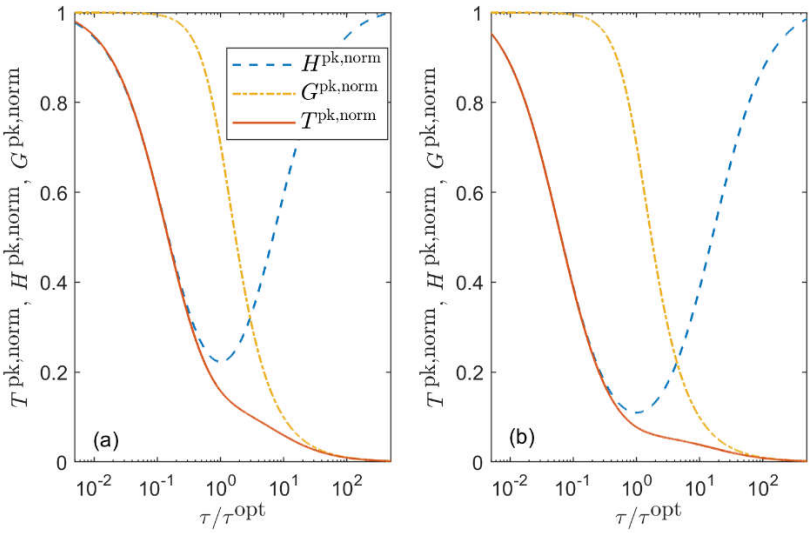

Figure 6: Trend of T^{pk}, H^{pk} and G^{pk} for OP-AMP output voltage with NC in series (Type A) for two different systems: $|k_i| = 0.1$ and $C_2 = (10/3)C_{\mathrm{pi}}$ (thus, $|\tilde{k}_i|/|k_i| = \sqrt{10/7}$) (a) and $|k_i| = 0.1$ and $C_2 = (10/7)C_{\mathrm{pi}}$ (thus, $|\tilde{k}_i|/|k_i| = \sqrt{10/3}$) (b). All the curves are normalized (as indicated by the superscript 'norm') in order to have 1 as maximum value in each plot for a straightforward comparison of the trends. $\xi_i = 10^{-3}$, $\omega_i/(2\pi)$ =30 Hz, $C_{\mathrm{pi}} = 30$ nF, $R_1 = 6$ kΩ (R_1/R_2 has no effect here).

Something similar occurs if the behaviour of the OP-AMP outputs is studied as a function of the NC value. When the values of either C_1 or C_2 get closer and closer to the value of C_{pi}, the attenuation performance increases because $|\tilde{k}_i|$ increases (see Table 1). This in turn implies that the mechanical vibrations decrease, leading to a decrease of the peak of $|H_i|$, thus with a favorable effect on the peak of $|T_i|$. Indeed, the comparison of Figure 6a and Figure 6b shows that when the value of $|\tilde{k}_i|$ increases (from plot (a) to plot (b)), the influence of $|H_i|$ on $|T_i|$ around $\tau = \tau^{\mathrm{opt}}$ becomes higher and higher; this is due to the higher and higher attenuation levels achieved. It must be pointed out that this does not mean that the global voltage output decreases from Figure 6a and Figure 6b (indeed, Figure 6 is normalised on the maximal values of the curves) but that the influence of the mechanical part on the output voltage becomes increasingly relevant as the NC value approaches the stability limit.

Figure 6 and its outcomes are related to NCs in series. For NCs in parallel, similar outcomes are found. The only difference is that the curves for NCs in parallel show an opposite trend as a function of τ/τ^{opt} compared to those shown in Figure 6. This means that, as an example, the curve of $G^{\mathrm{pk,norm}}$ is close to 1 for $\tau/\tau^{\mathrm{opt}} \gg 1$ and close to 0 for $\tau/\tau^{\mathrm{opt}} \ll 1$.

4.2 MDOF system

This subsection generalises the discussion presented in Section 4.1 to the case of an MDOF system.

For an MDOF system, each mode contributes to the OP-AMP output in a way that depends on the ratio between the used shunt resistance *R* (and, thus, the actual value of τ) and the optimal resistance for that mode (and, thus, its τ^{opt} value) (see Figure 6). Supposing, as an example, to control a low-order mode of an

MDOF system with an NC in series, in this configuration (i.e. resistive shunt with an NC in series) the value of τ^{opt} decreases with increasing the eigenfrequency of the target mode [49]. Therefore, if the τ value is set to control a low frequency mode, most of the other modes of the system will be characterised by a ratio τ/τ^{opt} higher than 1. It is possible to observe from Figure 6 that the value of T^{pk} decreases when τ/τ^{opt} increases for an NC in series, which is positive because this reduces the contribution to the OP-AMP outputs of the modes higher than the targeted one.

In light of this, in order to tune the circuit parameters in case of MDOF systems, the optimal τ (and thus *R*) value should be defined to control the target modes. Then, the NC parameters R_1 and R_1/R_2 should be optimized in order to minimize V_o (or/and I_o) according to the results shown in Table 2. Given this configuration, which is optimal for both the control performance and the OP-AMP outputs, it is possible to act on the *R* and NC values to further reduce the OP-AMP outputs if needed, knowing that this would lead to a decrease of the control performance.

However, it is possible to notice that a moderate increase of the *R* value can lead to a significant reduction of the OP-AMP outputs since it increases the value of τ/τ^{opt} for all the modes, without considerably deteriorating the attenuation of the targeted mode.

As an example, Figure 6a shows that, passing from τ/τ^{opt}=1 to τ/τ^{opt}=1.66 for the given mode, the value of T^{pk} decreases of approximately 20%, at the cost of an increase of H^{pk} of approximately 10%, thus leading to a reduction of the peak of the OP-AMP output which is, in percentage, twice than the loss of attenuation performance. This aspect can be easily understood by looking at Figure 7, which shows the vibration attenuation (of the peak of the amplitude of the displacement/force FRF) in decibel and T^{pk} as functions of $|\tilde{k}_i|$ and τ/τ^{opt} for a system chosen as an example. For a given value of $|\tilde{k}_i|$, the attenuation curves (red dotted lines) show a moderate slope around τ/τ^{opt}=1 and, therefore, a slight change of τ/τ^{opt} around the optimal ratio (i.e. 1) does not imply a significant loss of performance. Conversely, the blue solid curves, representing T^{pk}, are quite steep around τ/τ^{opt}=1 and, thus, the same change of τ leads to a non-negligible reduction of the OP-AMP output.

Another important aspect, which can be noticed looking at the curves of Figure 7, is the following. As mentioned, in the area of τ/τ^{opt} close to 1 the T^{pk} curves are steep (almost vertical in some cases). This means that a decrease of the $|\tilde{k}_i|$ value (or an increase as well) would just lead to a change of the control performance without significantly modifying the OP-AMP output. Nevertheless, if the desired reduction of T^{pk} can be obtained only with a significant increase of τ (e.g. from τ/τ^{opt}=1 to τ/τ^{opt}=10), thus leading to a drastic decrease of the achievable vibration attenuation (see the right side of Figure 7), it is convenient to modify the NC value (and thus decrease $|\tilde{k}_i|$), rather than increase τ (and, thus, *R*). Of course, this is an extreme situation which implies a significant loss of control performance and, thus, it would be better, if possible, to adopt a different OP-AMP with a higher output range.

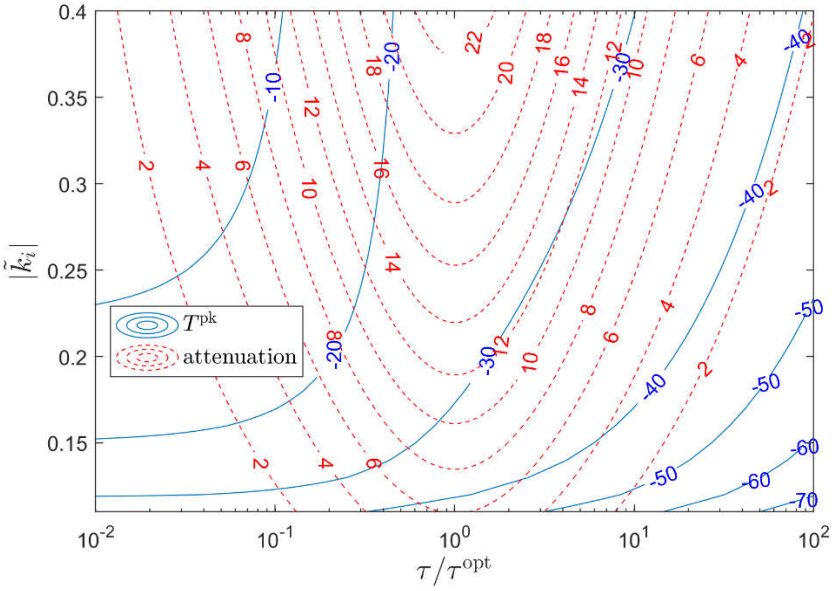

Figure 7: Iso-lines for the vibration attenuation calculated in decibel and for T^{pk} (in decibel) for OP-AMP output voltage with NC in series (Type B) as functions of the values of $|\tilde{k}_i|$ and τ/τ^{opt} for an SDOF system chosen as example ($|k_i|$ =0.1, $\xi_i = 3 \times 10^{-3}$, $\omega_i/(2\pi)$ =100 Hz, $C_{\mathrm{p}i} = 30$ nF, R_1/R_2=1.5, R_1 has no effect here). Considering T^{pk}, 0 dB corresponds to the maximum value in the plot. The attenuation is calculated (in decibel) as the ratio between the peak amplitude of the displacement/force FRF with the piezoelectric actuator in short-circuit and the peak amplitude of the displacement/force FRF controlled by means of the shunt.

Similar considerations can be deduced for NCs in parallel: they are used to attenuate high-order modes which require low values of τ^{opt}. Considering the modes at frequency lower than that for which τ/τ^{opt} is equal to 1 (which are the majority of the system modes), their τ/τ^{opt} values are lower than 1. According to Eqs. (21), (22), (27) and (28), and the last part of Section 4.1, low values of τ/τ^{opt} lead to a decrease of T^{pk}. Therefore, in this case, a slight decrease of *R* can provide significant benefits in terms of OP-AMP output with slight worsening of the attenuation performance for the mode which is the main target of the control.

However, to know whether the risk of OP-AMP saturation is real in a given application, this discussion is not enough. Indeed, the risk of saturation is related to the number of modes for which the value of τ/τ^{opt} is disadvantageous ($\tau/\tau^{\mathrm{opt}} \ll 1$ for an NC in series and $\tau/\tau^{\mathrm{opt}} \gg 1$ for an NC in parallel), to the value of the NC and to the power content of the disturbance as a function of frequency. Furthermore, another variable to be accounted for is the value of the eigenvectors of the modes for which the OP-AMP output is expected to be significant (see Eqs. (27) and (28), where the value of the eigenvector components is shown to influence the OP-AMP output). Therefore, to answer the question (and also to understand whether Type A or B circuit must be used, see Section 3), an MDOF model of the electro-mechanical system is necessary. Such a model is described in Section 5 in order to provide the reader with a tool for choosing the best configuration to reach a given level of vibration attenuation and, at the same time, to prevent (or reducing the risk of) OP-AMP saturation and reduce the circuit power consumption.

To summarise, Section 4, 4.1 and 4.2 have shown that in order to choose the proper NC circuit for reducing the OP-AMP outputs:

- the dynamics of the mechanical part of the electro-mechanical system must be taken into consideration;
- the value of *R* can be changed if necessary, because moderate changes can cause a significant decrease of the OP-AMP outputs with a slight worsening of the attenuation performance;
- an MDOF model of the electro-mechanical system is needed.

5 The MDOF model

This subsection explains how to derive the mentioned MDOF model. The frequency range of the first n modes (with $n < N$) is taken into account. The n modes considered are those in the frequency range where the power of the disturbance *F* is significant. According to Section 2.1, the equations of motion are described by limiting Eq. (1) to the modes of interest:

$$\ddot{q}_i + 2\xi_i\omega_i\dot{q}_i + \omega_i^2 q_i - \chi_i V = F_i \qquad \forall\, i \in \{1, \dots, n\} \tag{29}$$

Considering the electrical equation, it is not sufficient to limit the summation in Eq. (2) to the modes of interest but the contribution of the out-of-band modes must be taken into account in the $C_{\mathrm{p}n}$ term, leading to:

$$C_{\mathrm{p}n} V - Q + \sum_{i=1}^{n} \chi_i q_i = 0 \tag{30}$$

According to Eq. (29) (and applying the superimposition principle), it is possible to write the FRFs $L_i^{\mathrm{f}}(\mathrm{j}\Omega)$ between the external force *F* and the modal variables q_i, and the FRFs $L_i^{\mathrm{v}}(\mathrm{j}\Omega)$ between the voltage between the electrodes of the piezoelectric actuator *V* and the modal variables q_i:

$$L_i^{\mathrm{f}}(\mathrm{j}\Omega) = \frac{q_i}{F}(\mathrm{j}\Omega) = \frac{\Phi_i(x_{\mathrm{f}})}{-\Omega^2 + 2\mathrm{j}\xi_i\omega_i\Omega + \omega_i^2} \qquad \forall\, i \in \{1, \dots, n\} \tag{31}$$

$$L_i^{\mathrm{v}}(\mathrm{j}\Omega) = \frac{q_i}{V}(\mathrm{j}\Omega) = \frac{\chi_i}{-\Omega^2 + 2\mathrm{j}\xi_i\omega_i\Omega + \omega_i^2} \qquad \forall\, i \in \{1, \dots, n\} \tag{32}$$

Rearranging Eq. (30) using Eqs. (31) and (32) and the link between *V* and $\dot{Q}$ through Z_{sh} (see Figure 1), it is possible to write that:

$$\frac{V}{F}(\mathrm{j}\Omega) = \frac{-\sum_{i=1}^{n} \chi_i L_i^{\mathrm{f}}}{\left(C_{\mathrm{p}n} + \frac{1}{\mathrm{j}\Omega Z_{\mathrm{sh}}} + \sum_{i=1}^{n} \chi_i L_i^{\mathrm{v}}\right)} \tag{33}$$

Noticing that for a type A NC in parallel:

$$Z_{\mathrm{sh}} = \frac{R}{1 - \mathrm{j}\Omega R C_1}, \quad V_{\mathrm{o}} = V(1 + \mathrm{j}\Omega R_1 C_1), \quad I_{\mathrm{o}} = V\mathrm{j}\Omega C_1\left(1 + \frac{R_1}{R_2}\right) \tag{34}$$

for a type B NC in parallel:

$$Z_{\mathrm{sh}} = \frac{R}{1 - \mathrm{j}\Omega R C_1}, \quad V_{\mathrm{o}} = V(1 + \frac{R_2}{R_1}), \quad I_{\mathrm{o}} = V(\frac{1}{R_1} + \mathrm{j}\Omega C_1) \tag{35}$$

for a type A NC in series:

$$Z_{\mathrm{sh}} = R - \frac{1}{\mathrm{j}\Omega C_2}, \quad V_{\mathrm{o}} = \frac{V(1 + \mathrm{j}\Omega R_1 C_2)}{(1 - \mathrm{j}\Omega R C_2)}, \quad I_{\mathrm{o}} = \frac{V}{(1 - \mathrm{j}\Omega R C_2)} \mathrm{j}\Omega C_2 (1 + \frac{R_1}{R_2}) \tag{36}$$

for a type B NC in series:

$$Z_{\mathrm{sh}} = R - \frac{1}{\mathrm{j}\Omega C_2}, \quad V_{\mathrm{o}} = \frac{V}{(1 - \mathrm{j}\Omega R C_2)}(1 + \frac{R_2}{R_1}), \quad I_{\mathrm{o}} = \frac{V(\frac{1}{R_1} + \mathrm{j}\Omega C_2)}{(1 - \mathrm{j}\Omega R C_2)} \tag{37}$$

the FRFs between *F* and the OP-AMP outputs (T^{vo} and T^{io}) can be written as:

$$T_{\mathrm{pa}}^{\mathrm{vo}}(\mathrm{j}\Omega) = \frac{V_{\mathrm{o}}}{F}(\mathrm{j}\Omega) = \frac{-\mathrm{j}\Omega R(1 + \mathrm{j}\Omega R_1 C_1)\sum_{i=1}^{n} \chi_i L_i^{\mathrm{f}}}{\vartheta}, \qquad T_{\mathrm{pa}}^{\mathrm{io}}(\mathrm{j}\Omega) = \frac{I_{\mathrm{o}}}{F}(\mathrm{j}\Omega) = \frac{\Omega^2 R C_1 (1 + R_1/R_2)\sum_{i=1}^{n} \chi_i L_i^{\mathrm{f}}}{\vartheta} \tag{38}$$

$$T_{\mathrm{pb}}^{\mathrm{vo}}(\mathrm{j}\Omega) = \frac{V_{\mathrm{o}}}{F}(\mathrm{j}\Omega) = \frac{-\mathrm{j}\Omega R(1 + R_2/R_1)\sum_{i=1}^{n} \chi_i L_i^{\mathrm{f}}}{\vartheta}, \qquad T_{\mathrm{pb}}^{\mathrm{io}}(\mathrm{j}\Omega) = \frac{I_{\mathrm{o}}}{F}(\mathrm{j}\Omega) = \frac{-\mathrm{j}\Omega R[(1/R_1) + \mathrm{j}\Omega C_1]\sum_{i=1}^{n} \chi_i L_i^{\mathrm{f}}}{\vartheta} \tag{39}$$

$$T_{\mathrm{sa}}^{\mathrm{vo}}(\mathrm{j}\Omega) = \frac{V_{\mathrm{o}}}{F}(\mathrm{j}\Omega) = \frac{-(1 + \mathrm{j}\Omega R_1 C_2)\sum_{i=1}^{n} \chi_i L_i^{\mathrm{f}}}{\lambda}, \qquad T_{\mathrm{sa}}^{\mathrm{io}}(\mathrm{j}\Omega) = \frac{I_{\mathrm{o}}}{F}(\mathrm{j}\Omega) = \frac{-\mathrm{j}\Omega C_2 (1 + R_1/R_2)\sum_{i=1}^{n} \chi_i L_i^{\mathrm{f}}}{\lambda} \tag{40}$$

$$T_{\mathrm{sb}}^{\mathrm{vo}}(\mathrm{j}\Omega) = \frac{V_{\mathrm{o}}}{F}(\mathrm{j}\Omega) = \frac{-(1 + R_2/R_1)\sum_{i=1}^{n} \chi_i L_i^{\mathrm{f}}}{\lambda}, \qquad T_{\mathrm{sb}}^{\mathrm{io}}(\mathrm{j}\Omega) = \frac{I_{\mathrm{o}}}{F}(\mathrm{j}\Omega) = \frac{-[(1/R_1) + \mathrm{j}\Omega C_2]\sum_{i=1}^{n} \chi_i L_i^{\mathrm{f}}}{\lambda} \tag{41}$$

with

$$\vartheta = \mathrm{j}\Omega R\left(C_{\mathrm{p}n} - C_1\right) + 1 + \mathrm{j}\Omega R \sum_{i=1}^{n} \chi_i L_i^{\mathrm{v}}, \qquad \lambda = C_{\mathrm{p}n} - C_2 - \mathrm{j}\Omega R C_{\mathrm{p}n} C_2 + (1 - \mathrm{j}\Omega R C_2)\sum_{i=1}^{n} \chi_i L_i^{\mathrm{v}} \tag{42}$$

These FRFs allow to carry out the multi-mode analysis and to study the OP-AMP output behaviour taking into consideration the effect of the electro-mechanical system modes in the frequency range of interest. If the power content of *F* as a function of the frequency can be estimated, it is possible to compare NC circuits A and B in terms of the OP-AMP outputs, for a given NC configuration (series or parallel according to the order of the modes to be damped; see previously in the paper), in order to find which is the less demanding circuit for the application considered. This is possible by calculating the power-spectrum [61] of

the OP-AMP outputs. As an example, the power spectrum Ψ_{sa}^{vo} of the OP-AMP voltage output for an NC in series, layout type A, is:

$$\Psi_{sa}^{vo}(\Omega) = |T_{sa}^{vo}(j\Omega)|^2 \Psi^F(\Omega) \tag{43}$$

where Ψ^F is the power-spectrum of the force *F*.

Obviously, the summations in Eqs. (38) to (41) can be limited to the modes which are highly excited by the external force, avoiding to model those which are out of the main frequency band of the disturbance.

It is worth noticing that the FRFs from (38) to (41) allow to calculate also the electrical power ρ required from the OP-AMP. Therefore, it is possible to study how ρ changes as function of the values of τ and NC, and how the corresponding attenuation performance changes (see Eq. (26)). This allows for a choice of the values taking into consideration both the power requirements for the OP-AMP and the obtained attenuation performance.

This MDOF model, thus, allows to find which is the best configuration (i.e. type A or B, values of R_1 and R_1/R_2) in terms of OP-AMP demands, which is in turn useful for choosing the NC configuration which can prevent saturations. Furthermore, the same model allows to estimate how much the OP-AMP outputs can be reduced when a variation of the attenuation performance (due to a change of either the NC or *R*, or both) is accepted.

6 Guidelines

This section provides some guidelines about how to build a shunt circuit based on an NC coupled to a resistance taking into consideration both the vibration attenuation and the OP-AMP outputs. As mentioned, the OP-AMP outputs are functions of many different parameters such as, as examples, the frequency band of the external disturbance, the value of τ used that depends on the type of control strategy, the values of the eigenvector components for the modes in the frequency range of the disturbance. The same applies to the attenuation performance, which is strictly related to type of control needed (e.g. minimization of frequency peaks, minimization of the root mean square (RMS) value of the response vibration signal). Therefore, a number of variables are involved in the relationship linking OP-AMP outputs and attenuation performance. To facilitate the design of the shunt circuit based on NCs, a procedure is proposed, that is based on the MDOF model presented previously.

The first step is to define the value of the parameters that determine the control performance: the shunt resistance *R* and the NC. Then, the NC layout and the values of its components can be defined. In order to do this, the following steps can be followed for a generic MDOF system:

1. The frequency band (and possibly the extent) of the external forcing in operating conditions has to be estimated. This first step will allow to properly define the modal model of the electro-mechanical system and to have an idea about the NC layout which is the most reliable for the given application (see point 4 of this list). Furthermore, the knowledge of the external disturbances allows to estimate the OP-AMP output and, thus, to evaluate the risk of saturation (see point 5).
2. Then, the system has to be characterized:
    - The modal parameters ξ_i, ω_i and $\Phi_i$of the system with the piezoelectric actuator short-circuited have to be identified (e.g. using experimental modal analysis techniques). All the modes that are supposed to be significantly excited in operational conditions have to be characterized and included in the model of the electro-mechanical system.

- The coupling factor k_i (or χ_i) has to be determined (e.g. with a modal analysis with the piezoelectric actuator in both short- and open-circuit, see Section 7) as well as the modal capacitance $C_{\mathrm{p}i}$ (e.g. with either a fitting procedure [42,58] or other methods [57,58]). Also these two parameters have to be estimated for all the modes for which the external forcing is supposed to be significant.

3. Once the model of the electro-mechanical system is defined, it is possible to set the shunt resistance *R* and the NC in order to obtain the desired control performance:
   - The desired attenuation targets for the modes of interest have to be set as well as the minimum admissible performance.
   - The choice of the NC connection depends on the control target: NC in series is suitable for low-order modes, while NC in parallel has to be employed to control modes at high frequency. For modes in the middle area of the spectrum, both the layouts can be used with similar performances, or it is possible to employ more complex circuits (e.g. [41]) to further increase the attenuation levels.
   - Then, the NC value can be defined. If the aim of the control is to maximise the attenuation, the NC must be set close to the stability limits. Otherwise, its absolute value can be chosen as the maximum (for the series) or the minimum (for the parallel) which allows to reach the control target [49].
   - Then, the value of τ (and, thus, of *R*) can be set according to the desired target (e.g. maximization of the attenuation on a given mode, minimization of the displacement/force FRF peak on a given frequency range, minimization of the displacement RMS on a given frequency range). Different works in the literature already discuss criteria to set the value of τ depending on the target required (e.g. [22,38,49,62]). More in detail, Berardengo et al. [49] proposed a method for optimising the value of τ in case of mono-modal control depending on the value of the NC. When broadband control is required, according to the different target of the control (e.g. H_∞ and H_2 control), different strategies can be adopted (e.g. [49,62]). Usually, the optimal τ value for these cases is between the optimal τ values for the mono-modal control of the lowest and highest modes considered.
4. Once the controller is tuned, the NC circuit and its parameters can be defined:
   - Since it is not possible to define a priori which is the less demanding layout in terms of OP-AMP outputs, both A and B types have to be considered at first. The R_1 and R_1/R_2 values have to be set according to the results of Table 2: they have to be kept as low as possible for type A and as high as possible for type B. The thresholds for low values in type A and high values in type B, due to the non-ideal behaviour of the OP-AMP, must be checked experimentally (the authors are currently studying this point).
   - Afterwards, Eqs. (18) and (19) have to be used to compare the two layouts and to define the frequency ranges where type A is less demanding than type B and vice versa. Three possible cases can be recognized: (a) in case the power spectrum of the disturbance $\Psi^{\mathrm{F}}(\Omega)$ is expected to be significant only in the frequency range where type A is less demanding than type B, type A has to be chosen; (b) if $\Psi^{\mathrm{F}}(\Omega)$ is expected to be significant only in the frequency range where type B is less demanding than type A, type B must be used; (c) if, instead, $\Psi^{\mathrm{F}}(\Omega)$ is significant in both the frequency ranges, it is necessary to simulate the system using the MDOF model of Section 5 to define the best NC layout (either A or B) for the given application.
5. At this point, if the amplitude of the forcing term is known, it is possible to simulate the system with the model of Section 5 to estimate the OP-AMP outputs and evaluate the risk of saturation. Otherwise, it is possible to test the system experimentally in working conditions.

6. In case critical values of OP-AMP outputs emerged at point 5 of this list, or the OP-AMP experienced saturations during the test, an adjustment of the control parameters *R* and NC can be performed to decrease the OP-AMP outputs:
    - the value of *R* (and, thus, of τ) can be increased if an NC in series is used, or decreased if the NC is in parallel (see Section 4.2). This allows to decrease the outputs of the OP-AMP. The worsening of the vibration attenuation is either moderate or even negligible, depending on the case, if the increase/decrease of *R* is up to approximately 100 or 200% (actually, this threshold depends on the ratio $|\tilde{k}_i|/|k_i|$, see Figure 7). A higher change of *R* is not suggested because it could worsen a lot the attenuation performance without a strong decrease of the OP-AMP output (see Section 4.2).
    - In case the OP-AMP output is still too large after having changed *R* at the previous step (the OP-AMP output can be estimated with the model presented in Section 5), the NC value must be made farther from the stability limit (i.e. either increase of C_2 or decrease of C_1, see Section 4.2 and Table 1). If the new NC value (together with the corresponding optimal τ value) provides an attenuation performance which is still acceptable, the steps from 4 to 6 of this list must be repeated. This procedure can be repeated iteratively until satisfactory values of both attenuation and OP-AMP outputs are achieved.
    - If, finally, it is not possible to find NC and *R* values able to provide satisfactory attenuation performances and, at the same time, OP-AMP outputs low enough, a new OP-AMP able to provide higher outputs must be used. Obviously, this increases the cost of the whole set-up.
7. Obviously, this sixth point of the numbered list should be avoided if not necessary because it will lead to a decrease of the attenuation level. It is underlined that in many practical cases the use of the MDOF model presented in Section 5 is necessary because each different mode in the frequency range of the external disturbance will contribute to the OP-AMP output, and its own weight will be dependent on the corresponding $\Phi_i(x_f)$ value. It can also occur that a mode able to provide a large contribution to the OP-AMP output is not the target of the control action provided by the shunt. Therefore, in this case, since the OP-AMP output and the attenuation performance depend on different modes, only the use of the MDOF model allows to solve the problem finding the best trade-off between attenuation performance and OP-AMP outputs.

7 Experimental tests

This section aims at validating most of the theoretical results discussed in the previous sections of the paper. Section 7.1 describes the set-up used for the tests, while Sections 7.2 and 7.3 discuss the experimental results for the series and parallel NC connections, respectively.

7.1 Set-up

The test set-up was an aluminum cantilever beam (length 161 mm, width 25 mm and thickness 1.1 mm) with one piezoelectric patch (length 51 mm, width 25 mm and thickness 0.38 mm, material type: Quickpack™) bonded at the clamped end (see Figure 8). The modes considered for the tests were the first two bending modes. The cantilever beam was excited by a contactless electro-magnetic actuator, composed by a coil (where current flows) and a magnet bonded to the beam. The force was estimated measuring the current flowing into the coil by means of a current clamp. Indeed, this current was assumed proportional to the force exerted to the beam [63]. The excitation was of random nature between 20 and 250 Hz. The vibrational response of the beam was measured by a laser velocimeter. The NC was built in

each test using the schematics of Figure 3, using an OP-AMP Texas Instruments OPA445A. The OP-AMP was supplied with a constant voltage $\pm V_{pp}$ (with V_{pp}=30 V).

The OP-AMP output voltage was measured with a 24-bit acquisition module with anti-aliasing filter on board. The OP-AMP output current was measured adding a small resistance (i.e. 100 Ω) at the output of the OP-AMP and measuring the voltage drop between its terminals.

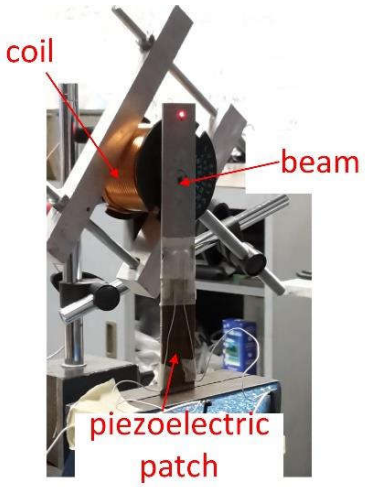

Figure 8: The experimental set-up.

The modal parameters of the two modes considered are provided in Table 3 and were identified by means of an experimental modal analysis. The value of $|k_i|$ was estimated as:

$$|k_i| \simeq \sqrt{\frac{\widehat{\omega}_i^2 - \omega_i^2}{\omega_i^2}} = k_{\text{eff}} \tag{44}$$

where $\widehat{\omega}_i$ is the open-circuit eigenfrequency of the electro-mechanical system without the addition of any NCs.

Moreover, Table 3 also presents the values of C_{p1} and C_{p2} obtained by measuring the capacitance of the piezoelectric transducer as a function of the frequency with an LCR meter [42,58]. The values of C_0 and C_∞ resulted equal to 49.85 and 30.86 nF, respectively.

It is noticed that, since the experimental tests presented in the following were carried out during different days, slight changes of the values of the parameters in Table 3 occurred for the different tests.

Table 3: Data of the test set-up identified experimentally.

Mode Number	$\omega_i/(2\pi)$ [Hz]	ξ_i [%]	$\lvert k_i \rvert$	$C_{\text{p}i}$ [nF]
1	29.46	0.47	0.155	48.72
2	181.64	0.37	0.078	48.43

7.2 Tests with an NC in series

In order to validate the outcomes related to the use of an NC in series, different tests were carried out and they are listed in Table 4. The test labels are reported in the first column of the table and the last letter of the test name indicates which NC type is considered: either type A or B.

When the value of the NC is set, the value of $|\tilde{k}_i|$ can be estimated by means of the values of ω_i^{oc} and ω_i^{sc} [49]:

$$|\tilde{k}_i| \simeq \sqrt{\frac{(\omega_i^{\mathrm{oc}})^2 - (\omega_i^{\mathrm{sc}})^2}{\omega_i^2}} \tag{45}$$

For most of the tests, the value of *R* was chosen in order to have $\tau = \tau^{\mathrm{opt}}$ for the first mode of Table 3 (i.e. tests from T1A to T4A). In addition, test T6B is related to *R* chosen in order to have $\tau = \tau^{\mathrm{opt}}$ for the second mode. According to [49], the value of τ^{opt} for a given mode can be calculated as:

$$\tau^{\mathrm{opt}} \simeq \frac{1}{\omega_i}\sqrt{\frac{2}{\tilde{k}_i^2 + 2}} \tag{46}$$

Once the value of C_{eq} is derived by means of the expressions in Table 1, the corresponding value of *R* is obtained using Eq. (20).

Tests T1 to T4 allow to evidence the effect of R_1 and R_1/R_2 on the OP-AMP outputs, without changing the attenuation performance (the values of *R* and the NC are not changed among these tests). Moreover, the comparison between tests T1A and T5A shows how a change of the NC value (and thus of the attenuation performance) is able to influence the OP-AMP outputs. In the following, all these points are treated in detail.

It is noticed that, for all the tests, the values of the different resistances of the shunt circuit were set using potentiometers. Each resistance value was measured with a multimeter before each test. Furthermore, the capacitance $\hat{C}$ was built with physical capacitors and, also in this case, their values were measured before each test.

Table 4: Tests performed with an NC in series.

Test name	Tested NC configurations	*R* [kΩ]	R_1 [kΩ]	$\frac{R_1}{R_2}$	R_2 [kΩ]	$\hat{C}$ [nF]	$\lvert\tilde{k}_1\rvert$	Vibration attenuation on mode 1 (num) [dB]	Vibration attenuation on mode 1 (exp) [dB]	Vibration attenuation on mode 2 (exp) [dB]
T1A	A	22.59	6	0.56	10.71	33.92	0.346	17.10	16.78	3.95
T1B	B	22.59	6	0.56	10.71	33.92	0.346	17.10	17.96	3.61
T2A	A	22.59	6	1.62	3.70	98.70	0.346	17.10	18.55	3.82
T2B	B	22.59	6	1.62	3.70	98.70	0.346	17.10	18.14	3.76
T3A	A	22.59	25	0.56	44.64	33.92	0.346	17.10	17.25	3.84
T3B	B	22.59	25	0.56	44.64	33.92	0.346	17.10	17.62	3.56
T4A	A	22.59	25	1.62	15.43	98.70	0.346	17.10	18.62	3.81
T4B	B	22.59	25	1.62	15.43	98.70	0.346	17.10	17.70	3.79
T5A	A	22.59	6	0.56	10.71	56.60	0.219	8.83	8.26	3.24
T6B	B	3.72	25	1.62	15.43	98.70	0.346	9.34	10.40	8.87

All the FRFs T_s^{vo} related to the OP-AMP voltage output shown in this subsection are reported in decibel and normalized over the same reference value. The value equal to 0 dB corresponds to the maximum value among all the FRFs from test T1A to T4B (i.e. the FRFs with the highest R and $|\tilde{k}_1|$ values). Therefore, all the FRFs related to the OP-AMP voltage output can be compared among the different figures of this subsection. The same applies to the FRFs related to the OP-AMP current output.

Figure 9 shows the effect of R_1 and R_1/R_2 on the outputs of a type A NC. Particularly, Figure 9a and Figure 9b show the effect of R_1 and R_1/R_2 on the voltage output, respectively, while Figure 9c and Figure 9d evidence the effect of R_1 and R_1/R_2 on the current output, respectively. All the figures show the experimental FRFs and the corresponding numerical FRFs computed with the model presented in Section 5. In all the cases, the match between the experimental and numerical curves is good and sometimes the curves cannot be distinguished in the plots. As expected from Section 3, an increase of R_1 increases the voltage output (plot a) but has no effect on the current output (plot c, where all the curves are almost superimposed), while an increase of R_1/R_2 increases the current output (plot d) but has no effect on the voltage output (plot b).

Similar comparisons are provided for a type B NC in Figure 10. Again, the results are in accordance with those of Section 3: an increase of R_1 decreases the current output (plot c) but has no effect on the voltage output (plot a), while an increase of R_1/R_2 decreases the voltage output (plot b) but has no effect on the current output (plot d).

In all the tests T1A to T4B, the attenuation performance is almost the same (see Table 4), as expected.

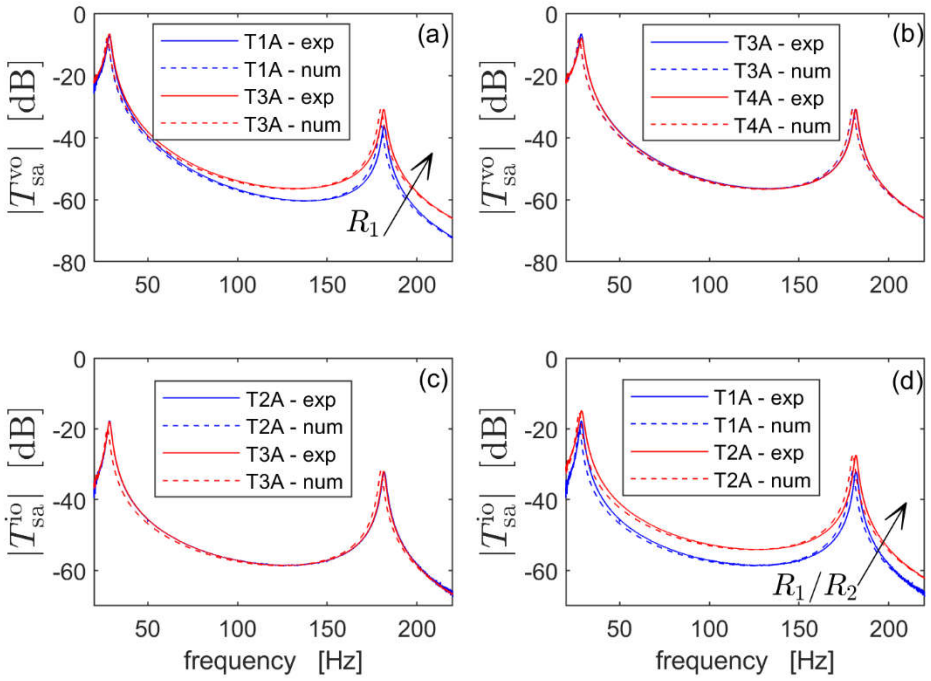

Figure 9: The effect of R_1 (plots a and c) and R_1/R_2 (plots b and d) on the OP-AMP outputs for a type A NC; the test labels are those of Table 4 (NC in series).

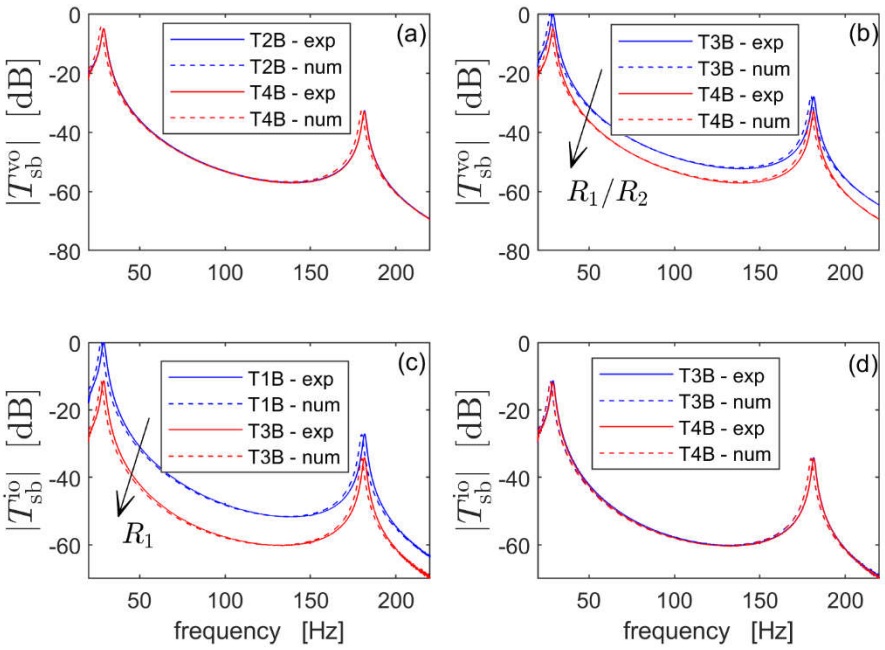

Figure 10: The effect of R_1 (plots a and c) and R_1/ R_2 (plots b and d) on the OP-AMP outputs for a type B NC; the test labels are those of Table 4 (NC in series).

Figure 11a shows a comparison in terms of OP-AMP current output between NCs in type A (T1A) and B (T3B). For the NC type A, the value of R_1/R_2 is the lowest used in the tests and this is favorable because, according to Table 2, the OP-AMP current output is minimised. For the NC type B, the value of R_1 is the highest used and, again, this is favorable in terms of OP-AMP current output according to Table 2. Figure 11a shows that at frequency values below approximately 80 Hz, type A is less demanding than type B in terms of current output, but at higher frequency values it becomes more demanding. This is again in agreement with Section 3, where it was shown that a frequency value exists where the type A NC passes from being less demanding than type B to being more demanding.

Figure 11b, instead, shows the effect of changing the NC value for a type A NC (tests T1A and T5A) in terms of current output. In test T5A, the value of $|\tilde{k}_1|$ is decreased by increasing the value of C_2, and the value of R is maintained optimal for the case of test T1A where $|\tilde{k}_1|$ is higher. The electric equations of the electro-mechanical system would indicate a decrease of the OP-AMP current output in test T5A due to an increase of C_2 (see Eq. (11)). However, since the vibration level of the first mode increases in test T5A (compared to test T1A, see the attenuation values in Table 4), because $|\tilde{k}_1|$ is lower and the R value is not optimal, the peak of $|T_{sa}^{io}|$ results higher in the case of test T5A. This proves the influence of the mechanical part of the electro-mechanical system, confirming that the mechanical behaviour of the electro-mechanical system must be properly taken into account for determining the OP-AMP outputs, as explained in Sections 4, 4.1 and 4.2.

Another interesting analysis is related to Figure 12. Plots (a) and (b) show the OP-AMP output voltage normalized over the supply voltage V_{pp} for test T1A (NC type A) and for test T4B (NC type B), respectively. A value close to 1 on the vertical axis means that saturation is close. In order to derive these figures, the disturbance force, that was equal for the two tests, was increased in order to have the most demanding configuration between the two of them close to saturation. In this case, the two configurations chosen were the best ones for both type A and B NCs: low value of R_1 for type A NC and high value of R_1/ R_2 for type B NC (see Table 2 and Table 4). According to Sections 3 and 4, since the disturbance is focused at low frequency and $|\Phi_1(x_f)| \gg |\Phi_2(x_f)|$, type A NC is expected to be less demanding than type B NC (see, as an

example, Figure 5). This is confirmed by the time histories shown in Figure 12a and Figure 12b (i.e. the time-history for type A in plot a shows lower peaks compared to that of type B in plot b).

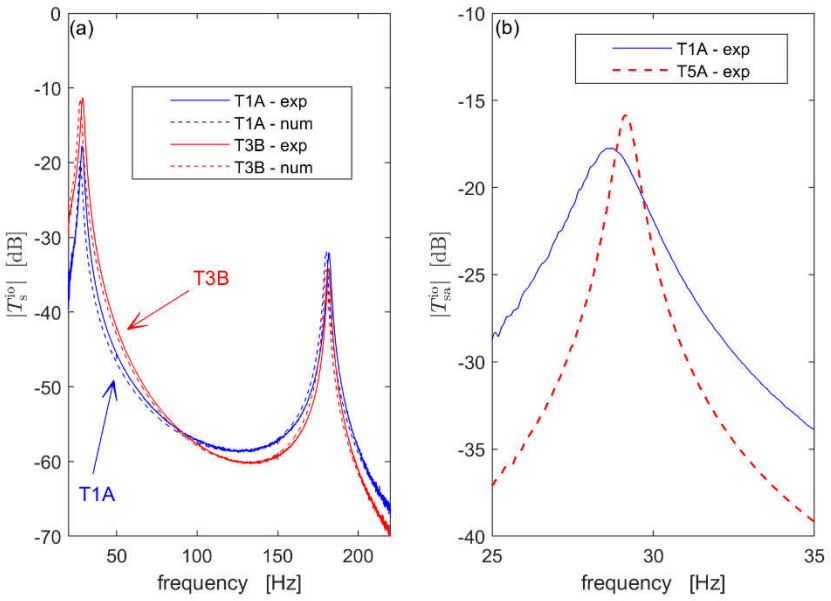

Figure 11: Comparison between Type A and B NCs in terms of OP-AMP current output with favorable values R_1/R_2 and R_1 for both the types (a) and comparison between tests T1A and T5A (type A NC), thus changing the value of the NC (b). The test labels are those of Table 4 (NC in series).

Figure 12c and Figure 12d show another comparison. In this case, plots (c) and (d) show the OP-AMP output voltage normalized over the supply voltage V_{pp} for a type B NC for tests T3B and T4B, respectively. Passing from test T3B to T4B implies an increase of the value of R_1/R_2 and, according to Table 2, this should make the NC less demanding in terms of OP-AMP output voltage. Again, in order to derive these figures, the disturbance force, which was equal for the two tests, was increased in order to have the most demanding configuration between the two of them close to saturation. The time-histories confirm that the increase of R_1/R_2 guarantees a significant decrease of the output voltage.

Finally, tests T4B and T6B are compared in Figure 13. The only difference between the two test configurations is related to the value of the shunt resistance R. In T4B, it is optimal for the first mode of the beam, while in T6B it is optimal for the second mode. In T4B R is higher than in T6B. Plots (a) and (b) shows that an increase of R allows to reduce current and voltage output, respectively, in agreement with the results of Section 4.1. A satisfactory match between experimental and numerical FRFs is found again. Figure 13c shows the trend of $T^{\mathrm{pk,norm}}$ for OP-AMP output voltage for modes 1 and 2 as function of τ/τ^{opt} (obtained using Eq. (27)), quantifying the benefit in terms of peak reduction of the FRF between the input force and the OP-AMP output voltage. For each of the two modes considered, the change of $T^{\mathrm{pk,norm}}$ when passing from their own optimal value of R to the optimal value for the other mode is quantified with the variable $y_{\mathrm{tp},i}$. More in detail, $y_{\mathrm{tp},i}$ is intended as the ratio $T_i^{\mathrm{pk,norm}}$ with $\tau \neq \tau^{\mathrm{opt}}$ over $T_i^{\mathrm{pk,norm}}$ with $\tau = \tau^{\mathrm{opt}}$. A value of y_{tp} higher than 1 means that $T^{\mathrm{pk,norm}}$ is increased passing from $\tau = \tau^{\mathrm{opt}}$ to $\tau \neq \tau^{\mathrm{opt}}$, while a value lower than 1 is related to a decrease of $T^{\mathrm{pk,norm}}$. As expected from the numerical simulations, mode 1 has a value of y_{tp} higher than 1 considering the R (and, thus, τ) values used in tests T4B and T6B, while mode 2 shows a value of y_{tp} lower than 1 (see Figure 13d). The experimental results are in accordance with the theoretical expectations.

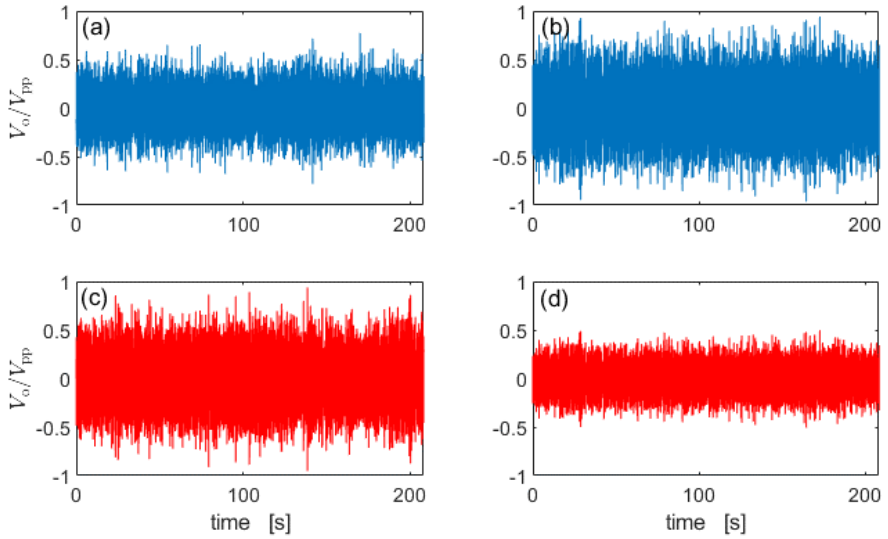

Figure 12: Time-histories of the OP-AMP output voltage normalized over the supply voltage V_{pp} for test T1A (a), test T4B (b), test T3B (c) and test T4B (d). The level of the disturbance force provided by the coil was different between tests T4B in plot b and T4B in plot d.

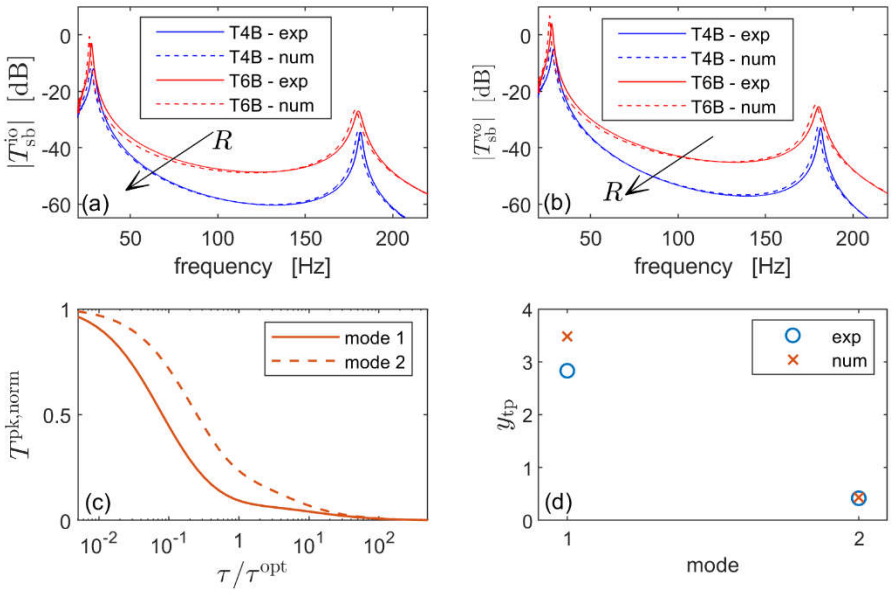

Figure 13: Comparison in terms of OP-AMP outputs between T4B and T6B to evidence the effect of *R* (plots a and b), trend of $T^{pk,norm}$ (for OP-AMP output voltage) for modes 1 and 2 as function of τ/τ^{opt} (c), and xperimental and numerical values of y_{tp} (for OP-AMP output voltage) for the same modes (d). The test labels are those of Table 4 (NC in series).

Before ending this subsection, it is worth evidencing two different points. The first is that, even if the two modes considered in the tests are in percentage far in frequency (i.e. $100(\omega_2/\omega_1)$>600), the shunt control allows to significantly attenuate both of them (see Table 4). The same applies to the tests for the NC in parallel presented in the next subsection. The second point is related to the importance of using the MDOF model to correctly design the shunt circuit. To this purpose, the results of two experiments related to cases chosen as examples are discussed here. The first is related to Tests T1A and T4B (which show the same attenuation values for the two modes considered in the tests) which have been repeated two further times, exciting the system using two different power spectral density (PSD) profiles for the current provided to the

exciting coil (see Figure 14a). Figure 14b shows that both the profiles are able to excite the first mode, on which the value of R is tuned, since the PSD of the vibration response of the structure shows in both cases a high peak in correspondence of the first eigenfrequency. However, profile 1 excites this mode more than profile 2. The two tests considered are designed to be favorable in terms of OP-AMP current output (i.e. low value of R_1/R_2 for T1A and high value of R_1 for T4B). To compare NC types A and B, the PSD of the OP-AMP current output in the two cases is reported in Figure 14c and Figure 14d for forcing profiles 1 and 2, respectively. With profile 1, the RMS value of the OP-AMP current output signal in T1A is approximately half than in T4B, thus evidencing an advantage provided by the use of type A. Conversely, with profile 2, the RMS value of the OP-AMP current output signal in T1A is larger than in T4B (approximately 30% larger), thus implying an advantage in using type B. This example allows to evidence again that a large number of parameters must be considered when designing the shunt circuit. Among them, there is the frequency profile of the external disturbance. In this context, it is important to use the proposed MDOF model for a proper design of the shunt circuit.

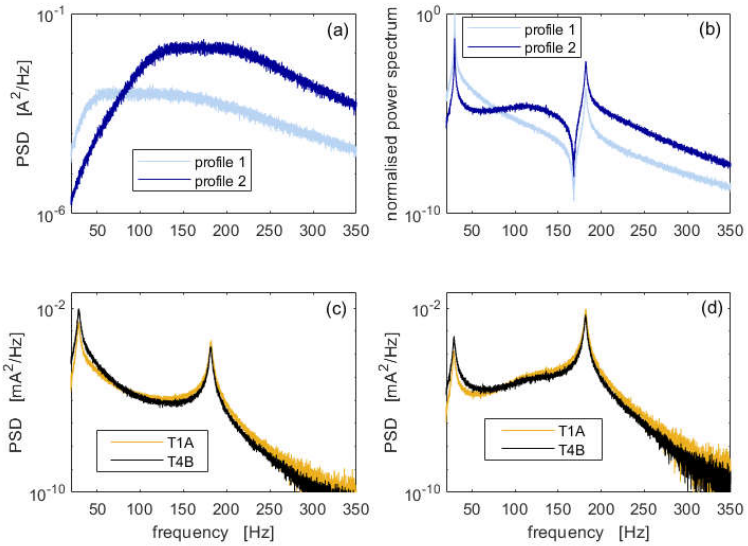

Figure 14: PSD profiles used for two repetitions of T1A and T4B (a), power spectrum of the vibration response of the structure for the two excitation profiles (the power spectra are normalised over the maximum displayed value for a straightforward percentage comparison, thus resulting in non-dimensional quantities; the two NC types provide similar response PSDs) (b) and PSDs of the OP-AMP current output for profile 1 (c) and 2 (d).

The second experimental example is related to a case in which the target is to attenuate the second mode and the external excitement profile is profile 2 in Figure 14a, where the first mode undergoes a lower excitation compared to the second. This excitement profile was used to repeat tests T4B and T6B. In this case, the forcing profile, the control target as well as the distance between the two modes would suggest to use an SDOF model for the electro-mechanical system. Figure 15a shows the attenuation on the amplitude peak of the second mode as a function of the adopted R value (from 1 to 30 kΩ). The optimal value is 3.72 kΩ (see also test T6B in Table 4). Here, the numerical curve has been derived using the approach presented in [49]. Figure 15b shows the RMS value of the OP-AMP output voltage V_O estimated with the MDOF model (accounting for the first two modes of the system) and the SDOF model (accounting only for the second mode of the system). The experimental results are shown for two different values of R: 3.72 kΩ (see test T6B) and 22.59 kΩ (i.e. the optimal value for the first mode, see test T4B). It is evident that the MDOF model is able to properly predict the RMS value, while the SDOF approach consistently underestimates the RMS value because it does not consider the fact that also the first mode of the structure contributes to the output. Moreover, it is interesting to notice that, if the RMS of the voltage

output is too high with *R* equal to 3.72 kΩ, it is possible to increase the value of *R* in order to decrease that of the RMS and this new tuning of *R* can be properly driven only by looking at the MDOF curve. This is a further evidence of the need to use the proposed MDOF model for a proper design of the shunt circuit.

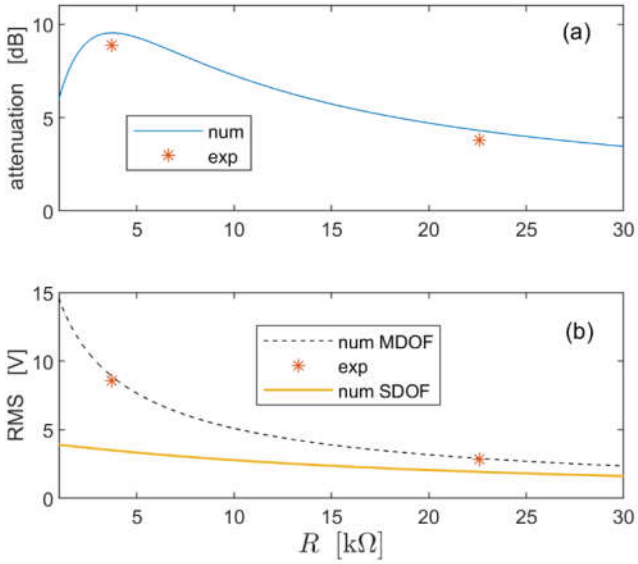

Figure 15: Numerical (lines) and experimental (asterisks) attenuation on the second mode of the beam as a function of the resistance *R* (a) and RMS value of the OP-AMP voltage output with external excitement profile equal to profile 2 in Figure 14a (b). The experimental results are related to tests T4B and T6B in Table 4.

7.3 Tests with an NC in parallel

This subsection treats the tests performed for the parallel NC. Different tests were carried out to evaluate the effect of the various circuit parameters on the OP-AMP outputs and they are reported in Table 5.

Tests T7 to T10 allow to evidence the effect of R_1 and R_1/R_2 on the OP-AMP outputs, without changing the attenuation performance. In tests from T7 to T10, the value of *R* was set in order to have $\tau = \tau^{\mathrm{opt}}$ for the first mode of Table 3. Instead, in T11, τ was chosen as optimal for the second mode of Table 3. Tests T7A, T7B, T11A and T11B have been thus compared to show how a change of the value of *R* is able to influence the OP-AMP outputs.

Table 5: Tests performed with an NC in parallel.

Test name	Tested NC configurations	R [kΩ]	R_1 [kΩ]	$\frac{R_1}{R_2}$	R_2 [kΩ]	$\hat{C}$ [nF]	$\lvert\tilde{k}_1\rvert$	Vibration attenuation on mode 1 (num) [dB]	Vibration attenuation on mode 1 (exp) [dB]	Vibration attenuation on mode 2 (exp) [dB]
T7A	A	219.20	6	0.50	12.00	12.22	0.219	11.02	9.92	2.13
T7B	B	219.20	6	0.50	12.00	12.22	0.219	11.02	9.67	1.90
T8A	A	219.20	6	1.97	3.05	48.00	0.219	11.02	9.93	2.19
T8B	B	219.20	6	1.97	3.05	48.00	0.219	11.02	9.72	2.10
T9A	A	219.20	25	0.50	50.00	12.22	0.219	11.02	10.03	2.24
T9B	B	219.20	25	0.50	50.00	12.22	0.219	11.02	9.85	2.12
T10A	A	219.20	25	1.97	12.69	48.00	0.219	11.02	9.57	2.18
T10B	B	219.20	25	1.97	12.69	48.00	0.219	11.02	9.92	2.12
T11A	A	36.29	6	0.50	12.00	12.22	0.219	5.16	4.98	4.95
T11B	B	36.29	6	0.50	12.00	12.22	0.219	5.16	4.85	4.63

All the FRFs $T_{\mathrm{p}}^{\mathrm{vo}}$ related to the OP-AMP voltage output shown in this subsection are reported in decibel and normalized over the same reference value. The value equal to 0 dB corresponds to the maximum value among all the FRFs from test T7A to T10B (i.e. the FRFs with the highest *R* value). Therefore, all the FRFs related to the OP-AMP voltage output can be compared among the different figures of this subsection. The same applies to the FRFs related to the OP-AMP current output.

Figure 16 shows some examples of the effects of R_1 and R_1/R_2 on the OP-AMP outputs: an increase (slight in the low frequency range, in accordance with Figure 4a) of V_o for type A is experienced when R_1 is increased (plot a), while V_o for type B decreases when R_1/R_2 is increased (plot b). Considering I_o, it increases for type B when R_1 decreases (plot c), while it increases when R_1/R_2 increases for type A (plot d). Again, a good match between experimental and theoretical results is achieved and the conclusions gathered in Table 2 are confirmed by the experimental results. It is also evidenced that the attenuation performance is almost the same in all these tests, as expected (see Table 5).

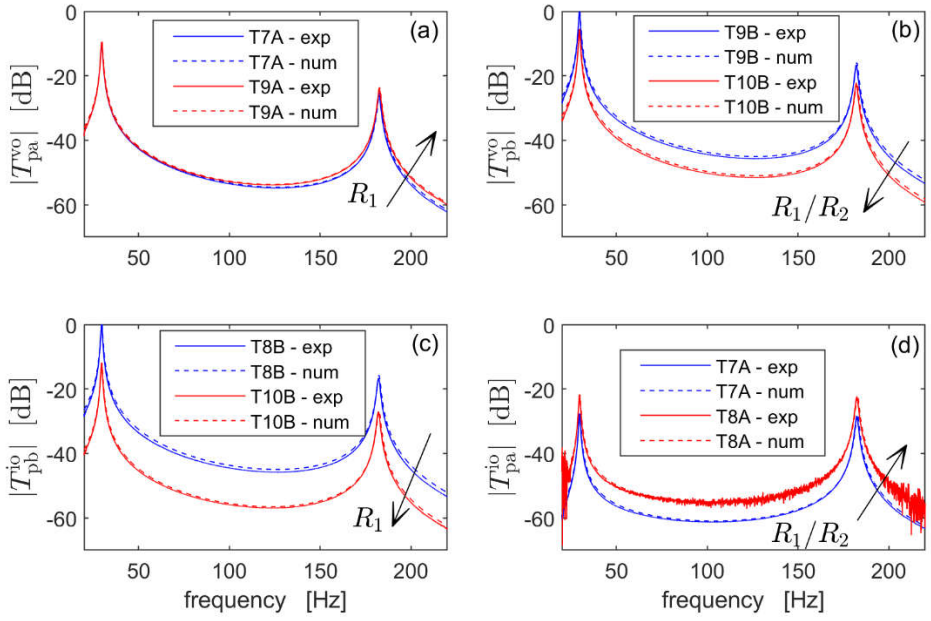

Figure 16: The effect of R_1 (plots a and c) and R_1/R_2 (plots b and d) on the OP-AMP outputs; the test labels are those of Table 5 (NC in parallel).

Furthermore, the effect of the value of the shunt resistance *R* on the OP-AMP outputs is shown in Figure 17, where the tests T7A, T7B, T11A and T11B are compared. According to this figure, it is possible to notice that, in the parallel case, a decrease of the value of *R* leads to a decrease of the OP-AMP outputs, as expected from Sections 4.2. This is mainly due to the behavior of the electrical part of the electro-mechanical system. Indeed, the last part of Section 4.2 explains that the value of G^{pk} for an NC in parallel decreases when τ/τ^{opt} decreases (i.e. passing from test T7 to test T11).

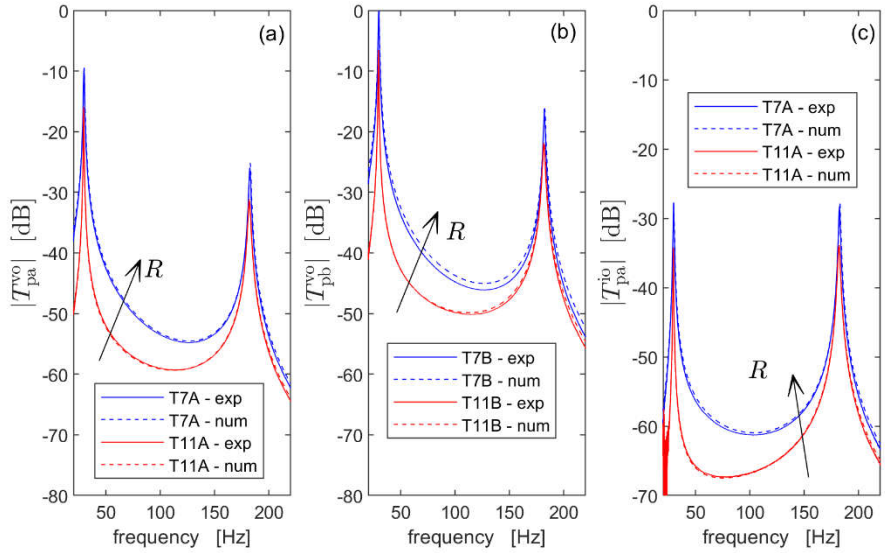

Figure 17: The effect of *R* on the OP-AMP voltage (a and b) and current (c) outputs.

8 Conclusion

This paper has addressed the piezoelectric shunt damping improved by the use of NCs from the OP-AMP output point of view. Indeed, NCs are built employing OP-AMPs and the paper has shown how it is possible to decrease their outputs by keeping the same level of vibration attenuation. Since it is possible to act separately on the OP-AMP voltage and current outputs, it is also possible to lower the power consumption of the NC circuit by properly tuning the values of the circuit elements. Furthermore, the paper has also analysed how to tune the shunt circuit components which also influence the attenuation provided by the control system.

Another important outcome of the paper is that the mechanical part of the electro-mechanical system cannot be neglected when assessing the OP-AMP outputs at frequency values around resonances.

Furthermore, two different possible circuits (A and B) used for building NCs have been compared, showing that there is no layout always less demanding than the other in terms of OP-AMP outputs. Therefore, an MDOF model of the electro-mechanical system is often required to understand which configuration of the NC has to be used in a given engineering application. Thus, the MDOF model has been developed and validated.

All the theoretical results have been compared to the results of an experimental campaign on a cantilever beam with a piezoelectric patch bonded at its clamped end. This comparison showed a good match between theoretical expectations and experimental results.

ACKNOWLEDGMENTS

This research has financially been supported at University of Parma by the Programme "FIL-Quota Incentivante" of University of Parma and co-sponsored by Fondazione Cariparma. Furthermore, the Italian Ministry of Education, University and Research is acknowledged by the staff of Politecnico di Milano for the

support provided through the Project "Department of Excellence LIS4.0 - Lightweight and Smart Structures for Industry 4.0".

REFERENCES

[1] H. Sun, Z. Yang, K. Li, B. Li, J. Xie, D. Wu, L. Zhang, Vibration suppression of a hard disk driver actuator arm using piezoelectric shunt damping with a topology-optimized PZT transducer, Smart Materials and Structures. 18 (2009) 065010. doi:10.1088/0964-1726/18/6/065010.

[2] B. Zhou, F. Thouverez, D. Lenoir, Vibration Reduction of Mistuned Bladed Disks by Passive Piezoelectric Shunt Damping Techniques, AIAA Journal. 52 (2014) 1194–1206. doi:10.2514/1.J052202.

[3] A. Sénéchal, O. Thomas, J.F. Deü, Optimization of shunted piezoelectric patches for vibration reduction of complex structures - Application to a turbojet fan blade, in: Proceedings of the ASME 2010 International Design Engineering Technical Conferences & Computers and Information in Engineering Conference IDETC/CIE - August 15-18 2010, Montreal (Canada), 2010: pp. 695–704. doi:10.1115/DETC2010-28737.

[4] N. Hagood, A. von Flotow, Damping of structural vibrations with piezoelectric materials and passive electrical networks, Journal of Sound and Vibration. 146 (1991) 243–268.

[5] P. Gardonio, D. Casagrande, Shunted piezoelectric patch vibration absorber on two-dimensional thin structures: Tuning considerations, Journal of Sound and Vibration. 395 (2017) 26–47. doi:10.1016/j.jsv.2017.02.019.

[6] O. Thomas, J. Ducarne, J.-F. Deü, Performance of piezoelectric shunts for vibration reduction, Smart Materials and Structures. 21 (2012) 015008. doi:10.1088/0964-1726/21/1/015008.

[7] G. Raze, B. Lossouarn, A. Paknejad, G. Zhao, J.-F. Deü, C. Collette, G. Kerschen, A multimodal nonlinear piezoelectric vibration absorber, in: Proceedings of ISMA 2018 - International Conference on Noise and Vibration Engineering and USD 2018 - International Conference on Uncertainty in Structural Dynamics, 17-19 September 2018, Leuven (Belgium), 2018: pp. 63–77.

[8] K. Marakakis, G.K. Tairidis, P. Koutsianitis, Shunt Piezoelectric Systems for Noise and Vibration Control : A Review, Frontiers in Built Environment. 5 (2019) 64. doi:10.3389/fbuil.2019.00064.

[9] K. Yamada, H. Matsuhisa, H. Utsuno, K. Sawada, Optimum tuning of series and parallel LR circuits for passive vibration suppression using piezoelectric elements, Journal of Sound and Vibration. 329 (2010) 5036–5057. doi:10.1016/j.jsv.2010.06.021.

[10] J. Høgsberg, S. Krenk, Calibration of piezoelectric RL shunts with explicit residual mode correction, Journal of Sound and Vibration. 386 (2017) 65–81. doi:10.1016/j.jsv.2016.08.028.

[11] P. Soltani, G. Kerschen, G. Tondreau, A. Deraemaeker, Tuning of a piezoelectric vibration absorber attached to a damped structure, Journal of Intelligent Material Systems and Structures. 28 (2017) 1115–1129. doi:10.1177/1045389X16666180.

[12] U. Andreaus, M. Porfiri, Effect of Electrical Uncertainties on Resonant Piezoelectric Shunting, Journal of Intelligent Material Systems and Structures. 18 (2007) 477–485. doi:10.1177/1045389x06067116.

[13] R. Darleux, B. Lossouarn, J.F. Deü, Passive self-tuning inductor for piezoelectric shunt damping considering temperature variations, Journal of Sound and Vibration. 432 (2018) 105–118. doi:10.1016/j.jsv.2018.06.017.

[14] G. Caruso, A critical analysis of electric shunt circuits employed in piezoelectric passive vibration

damping, Smart Materials and Structures. 10 (2001) 1059–1068. doi:10.1088/0964-1726/10/5/322.

[15] M. Berardengo, S. Manzoni, A.M. Conti, Multi-mode passive piezoelectric shunt damping by means of matrix inequalities, Journal of Sound and Vibration. 405 (2017) 287–305. doi:10.1016/j.jsv.2017.06.002.

[16] S. Behrens, S.O.R. Moheimani, a. J. Fleming, Multiple mode current flowing passive piezoelectric shunt controller, Journal of Sound and Vibration. 266 (2003) 929–942. doi:10.1016/S0022-460X(02)01380-9.

[17] A.J. Fleming, S. Behrens, S.O.R. Moheimani, Reducing the Inductance Requirements of Piezoelectric Shunt Damping Systems, Smart Materials and Structures. 12 (2003) 57–64. doi:10.1088/0964-1726/12/1/307.

[18] S. Wu, Method for multiple-mode shunt damping of structural vibration using a single PZT transducer, in: Proc. SPIE 3327, Smart Structures and Materials 1998: Passive Damping and Isolation, San Diego (USA), 1998.

[19] G. Raze, A. Paknejad, G. Zhao, C. Collette, G. Kerschen, Multimodal vibration damping using a simplified current blocking shunt circuit, Journal of Intelligent Material Systems and Structures Structures. 31 (2020) 1731–1747. doi:10.1177/1045389X20930103.

[20] F. Dell'Isola, C. Maurini, M. Porfiri, Passive damping of beam vibrations through distributed electric networks and piezoelectric transducers: Prototype design and experimental validation, Smart Materials and Structures. 13 (2004) 299–308. doi:10.1088/0964-1726/13/2/008.

[21] R. Darleux, B. Lossouarn, J.F. Deü, Broadband vibration damping of non-periodic plates by piezoelectric coupling to their electrical analogues, Smart Materials and Structures. 29 (2020) ID 054001. doi:10.1088/1361-665X/ab7948.

[22] B. de Marneffe, a Preumont, Vibration damping with negative capacitance shunts: theory and experiment, Smart Materials and Structures. 17 (2008) 035015. doi:10.1088/0964-1726/17/3/035015.

[23] M. Date, M. Kutani, S. Sakai, Electrically controlled elasticity utilizing piezoelectric coupling, Journal of Applied Physics. 87 (2000) 863–868. doi:10.1063/1.371954.

[24] J. Tang, K.W. Wang, Active-passive hybrid piezoelectric networks for vibration control: comparisons and improvement, Smart Materials and Structures. 10 (2001) 794–806.

[25] T. Sluka, P. Mokrý, Feedback control of piezoelectric actuator elastic properties in a vibration isolation system, Ferroelectrics. 351 (2007) 51–61.

[26] M. Pohl, Increasing the performance of negative capacitance shunts by enlarging the output voltage to the requirements of piezoelectric transducers, Journal of Intelligent Material Systems and Structures. 28 (2017) 1379–1390. doi:10.1177/1045389X16666181.

[27] M. Lallart, É. Lefeuvre, C. Richard, D. Guyomar, Self-powered circuit for broadband, multimodal piezoelectric vibration control, Sensors and Actuators, A: Physical. 143 (2008) 377–382. doi:10.1016/j.sna.2007.11.017.

[28] B. Bao, W. Tang, Semi-active vibration control featuring a self-sensing SSDV approach, Measurement: Journal of the International Measurement Confederation. 104 (2017) 192–203. doi:10.1016/j.measurement.2017.03.018.

[29] K. Dekemele, P. Van Torre, M. Loccufier, High-voltage synthetic inductor for vibration damping in resonant piezoelectric shunt, Journal of Vibration and Control. (2020) in press. doi:10.1177/1077546320952612.

[30] L. Yan, B. Bao, D. Guyomar, M. Lallart, Periodic structure with interconnected nonlinear electrical networks, Journal of Intelligent Material Systems and Structures. 28 (2017) 204–229. doi:10.1177/1045389X16649448.

[31] B. Bao, D. Guyomar, M. Lallart, Vibration reduction for smart periodic structures via periodic piezoelectric arrays with nonlinear interleaved-switched electronic networks, Mechanical Systems and Signal Processing. 82 (2017) 230–259. doi:10.1016/j.ymssp.2016.05.021.

[32] W. Zheng, B. Yan, H. Ma, R. Wang, J. Jia, L. Zhang, C. Wu, Tuning of natural frequency with electromagnetic shunt mass, Smart Materials and Structures. 28 (2019). doi:10.1088/1361-665X/aaf585.

[33] B. Yan, H. Ma, W. Zheng, B. Jian, K. Wang, C. Wu, Nonlinear Electromagnetic Shunt Damping for Nonlinear Vibration Isolators, IEEE/ASME Transactions on Mechatronics. 24 (2019) 1851–1860. doi:10.1109/tmech.2019.2928583.

[34] S. Zhou, C. Jean-Mistral, S. Chesné, Electromagnetic shunt damping with negative impedances: Optimization and analysis, Journal of Sound and Vibration. 445 (2019) 188–203. doi:10.1016/j.jsv.2019.01.014.

[35] F. Xie, Y. Su, W. Zhou, W.Z. Zhang, Design and evaluation of a shunted flexible piezoelectric damper for vibration control of cable structures, Smart Materials and Structures. 28 (2019). doi:10.1088/1361-665X/ab2c14.

[36] J.F. Toftekær, A. Benjeddou, J. Høgsberg, S. Krenk, Optimal piezoelectric resistive–inductive shunt damping of plates with residual mode correction, Journal of Intelligent Material Systems and Structures. 29 (2018) 3346–3370. doi:10.1177/1045389X18798953.

[37] C.H. Park, A. Baz, Vibration Control of Beams with Negative Capacitive Shunting of Interdigital Electrode Piezoceramics, Journal of Vibration and Control. 11 (2005) 331–346. doi:10.1177/107754605040949.

[38] S. Behrens, A.. J. Fleming, S.O.R. Moheimani, A broadband controller for shunt piezoelectric damping of structural vibration, Smart Materials and Structures. 18 (2003) 18–28.

[39] B.S. Beck, K.A. Cunefare, M. Collet, Response-based tuning of a negative capacitance shunt for vibration control, Journal of Intelligent Material Systems and Structures. 25 (2013) 1585–1595. doi:10.1177/1045389X13510216.

[40] M. Kodejška, P. Mokrý, V. Linhart, J. Václavik, T. Sluka, Adaptive vibration suppression system: An iterative control law for a piezoelectric actuator shunted by a negative capacitor, IEEE Transactions on Ultrasonics, Ferroelectrics, and Frequency Control. 59 (2012) 2785–2796. doi:10.1109/TUFFC.2012.2520.

[41] M. Berardengo, S. Manzoni, O. Thomas, C. Giraud-Audine, A new electrical circuit with negative capacitances to enhance resistive shunt damping, in: Proceedings of the ASME 2015 Conference on Smart Materials, Adaptive Structures and Intelligent Systems - SMASIS 2015 - September 21-23 2015, ISBN: 9780791857298, Colorado Springs (CO, USA), 2015: p. ID 8836. doi:10.1115/SMASIS2015-8836.

[42] M. Berardengo, S. Manzoni, O. Thomas, M. Vanali, Piezoelectric resonant shunt enhancement by negative capacitances: Optimisation, performance and resonance cancellation, Journal of Intelligent Material Systems and Structures. 29 (2018) 2581–2606. doi:10.1177/1045389X18770874.

[43] M. Neubauer, R. Oleskiewicz, K. Popp, T. Krzyzynski, Optimization of damping and absorbing performance of shunted piezo elements utilizing negative capacitance, Journal of Sound and Vibration. 298 (2006) 84–107. doi:10.1016/j.jsv.2006.04.043.

[44] M. Berardengo, S. Manzoni, O. Thomas, M. Vanali, Guidelines for the layout and tuning of piezoelectric resonant shunt with negative capacitances in terms of dynamic compliance , mobility and accelerance, Journal of Intelligent Material Systems and Structures. (2021) in press. doi:10.1177/1045389X20986991.

[45] M. Berardengo, O. Thomas, C. Giraud-Audine, S. Manzoni, Improved shunt damping with two negative capacitances: an efficient alternative to resonant shunt, Journal of Intelligent Material Systems and Structures. 28 (2017) 2222–2238. doi:10.1177/1045389X16667556.

[46] M. Berardengo, A. Cigada, S. Manzoni, M. Vanali, Vibration Control by Means of Piezoelectric Actuators Shunted with LR Impedances: Performance and Robustness Analysis, Shock and Vibration. 2015 (2015) ID 704265. doi:10.1155/2015/704265.

[47] M. Berardengo, S. Manzoni, M. Vanali, The Behaviour of Mistuned Piezoelectric Shunt Systems and Its Estimation, Shock and Vibration. 2016 (2016) 9739217. doi:10.1155/2016/9739217.

[48] J.W. Park, J.H. Han, Sensitivity analysis of damping performances for passive shunted piezoelectrics, Aerospace Science and Technology. 33 (2014) 16–25. doi:10.1016/j.ast.2013.12.010.

[49] M. Berardengo, O. Thomas, C. Giraud-Audine, S. Manzoni, Improved resistive shunt by means of negative capacitance: new circuit, performances and multi-mode control, Smart Materials and Structures. 25 (2016) 075033. doi:10.1088/0964-1726/25/7/075033.

[50] P. Horowitz, W. Hill, The art of electronics, 2nd edition, Cambridge University Press, Cambridge, 1989.

[51] B.S. Beck, K.A. Cunefare, M. Collet, The power output and efficiency of a negative capacitance shunt for vibration control of a flexural system, Smart Materials and Structures. 22 (2013) 065009. doi:10.1088/0964-1726/22/6/065009.

[52] E.M. Qureshi, X. Shen, L. Chang, Power output and efficiency of a negative capacitance and inductance shunt for structural vibration control under broadband excitation, International Journal of Aeronautical and Space Sciences. 16 (2015) 223–246. doi:10.5139/IJASS.2015.16.2.223.

[53] J. Václavík, P. Mokrý, Measurement of mechanical and electrical energy flows in the semiactive piezoelectric shunt damping system, Journal of Intelligent Material Systems and Structures. 23 (2012) 527–533. doi:10.1177/1045389X12436730.

[54] J. Václavík, M. Kodejška, P. Mokrý, Wall-plug efficiency analysis of semi-active piezoelectric shunt damping systems, JVC/Journal of Vibration and Control. 22 (2014) 2582–2590. doi:10.1177/1077546314548910.

[55] O. Thomas, J. Deü, J. Ducarne, Vibrations of an elastic structure with shunted piezoelectric patches: efficient finite element formulation and electromechanical coupling coefficients, International Journal for Numerical Methods in Engineering. 80 (2009) 235–268. doi:10.1002/nme.

[56] J. Ducarne, O. Thomas, J.-F. Deü, Placement and dimension optimization of shunted piezoelectric patches for vibration reduction, Journal of Sound and Vibration. 331 (2012) 3286–3303. doi:10.1016/j.jsv.2012.03.002.

[57] J.F. Toftekaer, J. Hogsberg, Multi-mode piezoelectric shunt damping with residual mode correction by evaluation of modal charge and voltage, Journal of Intelligent Material Systems and Structures. 31 (2019) 570–586. doi:10.1177/1045389X19891646.

[58] M. Berardengo, S. Manzoni, J. Høgsberg, M. Vanali, Vibration control with piezoelectric elements: the indirect measurement of the modal capacitance and coupling factor, Mechanical Systems and Signal Processing. 151 (2021) 107350. doi:10.1016/j.ymssp.2020.107350.

[59] S. Moheimani, A. Fleming, Piezoelectric transducers for vibration control and damping, Springer, London, 2006.

[60] S. Manzoni, S. Moschini, M. Redaelli, M. Vanali, Vibration attenuation by means of piezoelectric transducer shunted to synthetic negative capacitance, Journal of Sound and Vibration. 331 (2012) 4644–4657. doi:10.1016/j.jsv.2012.05.014.

[61] A. Brandt, Noise and vibration analysis - Signal analysis and experimental procedures, Wiley, 2011.

[62] C. Bricault, C. Pézerat, M. Collet, A. Pyskir, P. Perrard, G. Matten, V. Romero-García, Multimodal reduction of acoustic radiation of thin plates by using a single piezoelectric patch with a negative capacitance shunt, Applied Acoustics. 145 (2019) 320–327. doi:10.1016/j.apacoust.2018.10.016.

[63] O. Thomas, C. Touzé, a. Chaigne, Asymmetric non-linear forced vibrations of free-edge circular plates. Part II: experiments, Journal of Sound and Vibration. 265 (2003) 1075–1101. doi:10.1016/S0022-460X(02)01564-X.

LIST OF TABLE CAPTIONS

Table 1: Definition of C_{eq}, ω_i^{sc}, ω_i^{oc} and $\tilde{k}_i$ [49].

Table 2: Effect of R_1 and R_1/R_2 on the OP-AMP outputs for an NC in either parallel or series connection.

Table 3: Data of the test set-up identified experimentally.

Table 4: Tests performed with an NC in series.

Table 5: Tests performed with an NC in parallel.

LIST OF FIGURE CAPTIONS

Figure 1: A generic forced structure with a piezoelectric patch shunted with an electric impedance Z_{sh}.

Figure 2: Parallel (a) and series (b) connection of the shunt impedance made from an NC and a resistance.

Figure 3: Physical implementation of NCs: type PA (a), type PB (b), type SA (c) and type SB (d).

Figure 4: Trend of M^{vo} and M^{io} as a function of R_1 and R_1/R_2 (valid for both series and parallel NC). The values on the vertical axes are normalized (as indicated by the word 'norm' in the superscript) in order to have a value equal to 1 for the highest value of each curve. $M_{\text{a}}^{\text{vo,norm}}$ (a), $M_{\text{b}}^{\text{vo,norm}}$ (b), $M_{\text{b}}^{\text{io,norm}}$ (c) and $M_{\text{a}}^{\text{io,norm}}$ (d). The absolute value of the NC is 40 nF.

Figure 5: Trend D^{vo} (a) and D^{io} (b) (valid for both series and parallel NC connections) as a function of the frequency for an NC absolute value equal to 40 nF (solid line) and 200 nF (dashed line), $R_1 = 6\ \text{k}\Omega$ and $R_1/R_2 = 1.5$.

Figure 6: Trend of T^{pk} (red solid line), H^{pk} (blue dashed line) and G^{pk} (orange dash-dotted line) for OP-AMP output voltage with NC in series (Type A) for two different systems: $|k_i| = 0.1$ and $C_2 = (10/3)C_{\mathrm{p}i}$ (thus, $|\tilde{k}_i|/|k_i| = \sqrt{10/7}$) (a) and $|k_i| = 0.1$ and $C_2 = (10/7)C_{\mathrm{p}i}$ (thus, $|\tilde{k}_i|/|k_i| = \sqrt{10/3}$) (b). All the curves are normalized (as indicated by the superscript 'norm') in order to have 1 as maximum value in each plot for a straightforward comparison of the trends. $\xi_i = 10^{-3}$, $\omega_i/(2\pi)$ =30 Hz, $C_{\mathrm{p}i} = 30$ nF, $R_1 = 6\ \mathrm{k\Omega}$ (R_1/R_2 has no effect here).

Figure 7: Iso-lines for the vibration attenuation calculated in decibel and for T^{pk} (in decibel) for OP-AMP output voltage with NC in series (Type B) as functions of the values of $|\tilde{k}_i|$ and τ/τ^{opt} for an SDOF system chosen as example ($|k_i|$ =0.1, $\xi_i = 3 \times 10^{-3}$, $\omega_i/(2\pi)$ =100 Hz, $C_{\mathrm{p}i} = 30$ nF, R_1/R_2=1.5, R_1 has no effect here). Considering T^{pk}, 0 dB corresponds to the maximum value in the plot. The attenuation is calculated (in decibel) as the ratio between the peak amplitude of the displacement/force FRF with the piezoelectric actuator in short-circuit and the peak amplitude of the displacement/force FRF controlled by means of the shunt.

Figure 8: The experimental set-up.

Figure 9: The effect of R_1 (plots a and c) and R_1/R_2 (plots b and d) on the OP-AMP outputs for a type A NC; the test labels are those of Table 4 (NC in series).

Figure 10: The effect of R_1 (plots a and c) and R_1/R_2 (plots b and d) on the OP-AMP outputs for a type B NC; the test labels are those of Table 4 (NC in series).

Figure 11: Comparison between Type A and B NCs in terms of OP-AMP current output with favorable values R_1/R_2 and R_1 for both the types (a) and comparison between tests T1A and T5A (type A NC), thus changing the value of the NC (b). The test labels are those of Table 4 (NC in series).

Figure 12: Time-histories of the OP-AMP output voltage normalized over the supply voltage V_{pp} for test T1A (a), test T4B (b), test T3B (c) and test T4B (d). The level of the disturbance force provided by the coil was different between tests T4B in plot b and T4B in plot d.

Figure 13: Comparison in terms of OP-AMP outputs between T4B and T6B to evidence the effect of R (plots a and b), trend of $T^{\mathrm{pk,norm}}$ (for OP-AMP output voltage) for modes 1 and 2 as function of τ/τ^{opt} (c), and experimental and numerical values of y_{tp} (for OP-AMP output voltage) for the same modes (d). The test labels are those of Table 4 (NC in series).

Figure 14: PSD profiles used for two repetitions of T1A and T4B (a), power spectrum of the vibration response of the structure for the two excitation profiles (the power spectra are normalised over the maximum displayed value for a straightforward percentage comparison, thus resulting in non-dimensional quantities; the two NC types provide similar response PSDs) (b) and PSDs of the OP-AMP current output for profile 1 (c) and 2 (d).

Figure 15: Numerical (lines) and experimental (asterisks) attenuation on the second mode of the beam as a function of the resistance R (a) and RMS value of the OP-AMP voltage output with external excitement profile equal to profile 2 in Figure 14a (b). The experimental results are related to tests T4B and T6B in Table 4.

Figure 16: The effect of R_1 (plots a and c) and R_1/R_2 (plots b and d) on the OP-AMP outputs; the test labels are those of Table 5 (NC in parallel).

Figure 17: The effect of *R* on the OP-AMP voltage (a and b) and current (c) outputs.